

# JGR Biogeosciences

## RESEARCH ARTICLE

10.1029/2023JG007482

### Key Points:

- Human activities changed the biospheric and petrogenic terrestrial particulate organic carbon (POC) flux from the Pearl River into the South China Sea during the last century
- Petrogenic POC burial flux increased by ~140% since the 1970s due to accelerating dam construction and likely coal consumption
- Fresh terrestrial biospheric POC burial increased since the 1950s due to intensified land use changes and river management

### Supporting Information:

Supporting Information may be found in the online version of this article.

### Correspondence to:

G. Mollenhauer and G. Jia,  
[gesine.mollenhauer@awi.de](mailto:gesine.mollenhauer@awi.de);  
[jiagd@tongji.edu.cn](mailto:jiagd@tongji.edu.cn)

### Citation:

Wei, B., Mollenhauer, G., Kusch, S., Hefter, J., Grotheer, H., Schefuß, E., et al. (2023). Anthropogenic perturbations change the quality and quantity of terrestrial carbon flux to the coastal ocean. *Journal of Geophysical Research: Biogeosciences*, 128, e2023JG007482. <https://doi.org/10.1029/2023JG007482>

Received 15 MAR 2023

Accepted 27 SEP 2023

### Author Contributions:

**Conceptualization:** Bingbing Wei, Gesine Mollenhauer, Guodong Jia  
**Formal analysis:** Bingbing Wei, Jens Hefter, Hendrik Grotheer, Enno Schefuß  
**Funding acquisition:** Bingbing Wei, Guodong Jia  
**Investigation:** Bingbing Wei, Stephanie Kusch  
**Methodology:** Bingbing Wei, Jens Hefter, Hendrik Grotheer, Enno Schefuß, Walter Geibert, Daniela Ransby  
**Writing – original draft:** Bingbing Wei  
**Writing – review & editing:** Bingbing Wei, Gesine Mollenhauer, Stephanie Kusch, Enno Schefuß, Walter Geibert, Daniela Ransby, Guodong Jia

## Anthropogenic Perturbations Change the Quality and Quantity of Terrestrial Carbon Flux to the Coastal Ocean

Bingbing Wei<sup>1,2</sup> , Gesine Mollenhauer<sup>2,3,4</sup> , Stephanie Kusch<sup>5</sup> , Jens Hefter<sup>2</sup> , Hendrik Grotheer<sup>2,4</sup> , Enno Schefuß<sup>4</sup> , Walter Geibert<sup>2</sup> , Daniela Ransby<sup>2,4</sup> , and Guodong Jia<sup>1,6</sup> 

<sup>1</sup>State Key Laboratory of Marine Geology, Tongji University, Shanghai, China, <sup>2</sup>Helmholtz Centre for Polar and Marine Research, Alfred Wegener Institute, Bremerhaven, Germany, <sup>3</sup>Department of Geosciences, University of Bremen, Bremen, Germany, <sup>4</sup>MARUM–Center for Marine Environmental Sciences, University of Bremen, Bremen, Germany, <sup>5</sup>ISMER–Institute des Sciences de la Mer de Rimouski, University of Quebec Rimouski, Rimouski, QC, Canada, <sup>6</sup>Southern Marine Science and Engineering Guangdong Laboratory (Zhuhai), Zhuhai, China

**Abstract** Human activities have increasingly changed terrestrial particulate organic carbon (POC) export to the coastal ocean since the Industrial Age (19th century). However, the influence of human perturbations on the composition and flux of terrestrial biospheric and petrogenic POC sub-pools remains poorly constrained. Here, we examined <sup>13</sup>C and <sup>14</sup>C compositions of bulk POC and source-specific biomarkers (fatty acids, FA) from two nearshore sediment cores collected in the Pearl River-derived mudbelt, to determine the impacts of human perturbations of the Pearl River watershed on the burial of terrestrial POC in the coastal ocean over the last century. Our results show that although agricultural practices and deforestation during the 1930s–1950s increased C<sub>4</sub> plant coverage in the watershed, the export fluxes of terrestrial biospheric and petrogenic POC remained rather unchanged; however, added perturbations since 1974, including increasing coal consumption, embankment and dam constructions caused massive export of both petrogenic POC and relatively fresh terrestrial biospheric POC from the river delta. Our data reveal that human activities substantially enhance the transfer of petrogenic POC and fresh biospheric POC to the coastal ocean after ca. 1974, with the latter process acting as an important sink for anthropogenic CO<sub>2</sub>.

**Plain Language Summary** The transport and deposition of carbon from land to the ocean through rivers is known to have an effect on CO<sub>2</sub> in the atmosphere. Yet, the impact of human activity on this process is poorly constrained. We use carbon isotope compositions of particulate organic carbon (POC) exported by the Pearl River to demonstrate that now, human activities exert an important control on the quantity and quality of terrestrial POC fluxes to the coastal ocean. Our findings reveal that different terrestrial carbon pools, namely biospheric POC eroded from plants and soils and petrogenic POC from fossil sources, responded strongly and independently to human activities in the catchment.

## 1. Introduction

Photosynthesis-derived particulate organic carbon (POC) burial in marine sediments efficiently draws down atmospheric carbon dioxide (CO<sub>2</sub>) in concert with silicate weathering on land (Galy & Eglinton, 2011; Hilton & West, 2020). Rivers transfer ~200 Tg C yr<sup>-1</sup> of terrestrial POC to the ocean, which represents an admixture of two sources, that is, biospheric POC fixed via photosynthesis and petrogenic POC stored in rocks, respectively (Galy et al., 2015). Relatively recently synthesized terrestrial POC can be reactive and hence be partially remineralized during transport and sedimentation, resulting in recycling of carbon to the atmosphere. Only the burial of biospheric POC that escapes remineralization in coastal sediments leads to sequestration of atmospheric CO<sub>2</sub> (Galy et al., 2015; Tao et al., 2015). In contrast, transport and reburial of terrestrial petrogenic POC exerts a minimal net effect on atmospheric CO<sub>2</sub>, but remineralization of this POC pool can lead to increased atmospheric CO<sub>2</sub> (Galy et al., 2015). The burial of terrestrial POC in coastal sediments also provides some of the most continuous and long-term records of past climate and carbon-cycle dynamics on the continents (Regnier et al., 2013). Yet, increasing human perturbation strongly affects the lateral terrestrial POC transfer to the coastal ocean and, in turn, the atmospheric CO<sub>2</sub> level.

Since the Industrial Age (i.e., the 19th century), land use changes (related to agriculture, urbanization and deforestation) and river management (e.g., damming and embankment) have accelerated (Regnier et al., 2022;

Syvitski et al., 2022). Land use changes associated with agricultural practices, urbanization and deforestation that enhance soil erosion should, in theory, increase terrestrial POC delivery to the river, whereas river management, in general, should impede/reduce terrestrial POC export from upland areas and riverbanks (Regnier et al., 2013; Syvitski et al., 2005), leading to decreased supply of petrogenic POC from natural rock weathering or deep soil erosion. However, this reduction may be offset by anthropogenic mobilization of petrogenic POC from other sources. For example, coal-fired power plants produce a considerable amount of coal fly ash (i.e., the residuum of coal burning), which has been suggested to be another important source of petrogenic POC to the coastal ocean (Li et al., 2021). This process is particularly important in China where coal consumption has increased since the 1950s and accounts for as much as ~50% of worldwide consumption nowadays (Z. T. Yao et al., 2015). However, the combined influence of the human activities outlined above on terrestrial POC export to the coastal ocean remains poorly understood, specifically for the biospheric and petrogenic POC sub-pools, and is mostly unaccounted for in natural settings, particularly when human activities are associated with climatic changes. Constraining these processes can not only further our understanding of the anthropogenic CO<sub>2</sub> budget and the effect of human perturbations on the coastal carbon sink, but also help closing the carbon budget of the ongoing anthropogenic perturbation (Bauer et al., 2013; Regnier et al., 2013). Here, we study the Pearl River (PR) and adjacent coastal systems to directly reveal human perturbations of terrestrial biospheric and petrogenic POC export to the ocean during the last century, a period of profound land use changes and river management.

The Pearl River originates from the Yunan-Guizhou Plateau, crosses mountainous and hilly areas, and flows into the northern South China Sea through the PR delta (Ge et al., 2014). From the river estuary to the Leizhou Peninsula, the PR-derived sediments are mainly distributed toward the southwest by the coastal current and deposited along the inner shelf (Figure 1a; Ge et al., 2014). The upper PR basin mostly consists of Cambrian to Triassic carbonates, whereas Precambrian metamorphic and magmatic rocks interspersed with Jurassic sedimentary rocks (shales and red sandstones) dominate the bedrock in the middle and lower basins (Figure 1b; Lin et al., 2019). A (sub)tropical monsoon climate dominates the PR basin, and its main vegetation today consists of agricultural plants (e.g., rice, sugar cane, and corn) and subtropical evergreen broad-leaved and coniferous forests with minor presence of grasses (Figure 1c; Yu et al., 2010). Human activities have progressively affected the PR watershed since the last century, including wartime deforestation during the 1940s, intensification and industrialization of agriculture since the 1950s, increased damming and embankment since the 1960s, and accelerated urbanization and industrialization after 1978 (Wu et al., 2012). At present, ~37% of the PR catchment land cover is classified as croplands and urban/built-up (Figure 1c), reflecting how substantially the watershed has been altered over the last century. According to a recent water census, as of 2013 a total length of 28,900 km in the lower basin has been embanked (MWR & NBS, 2013), indicating the enormous extent of river management activities. In contrast to such geospatial monitoring, variations of terrestrial biospheric and petrogenic POC export under recent human forcing remain largely unexplored, attributable to the lack of a reliable source assignment of sedimentary POC to different terrestrial pools as well as aquatic production. This knowledge gap can be filled by determining <sup>13</sup>C and <sup>14</sup>C compositions of bulk OC and biomolecular compounds unique to terrestrial biospheric POC (e.g., long-chain fatty acids forming the epicuticular wax of vascular plants) in river-influenced coastal sediments (Galy et al., 2007; Goñi, 1997; Kusch et al., 2010, 2021; Lin et al., 2019; Tao et al., 2015, 2016), allowing the calculation of biospheric and petrogenic POC burial fluxes.

We performed <sup>13</sup>C and <sup>14</sup>C analyses of bulk OC and fatty acids (FAs) from two nearshore sediment cores collected on the northern South China Sea shelf, with high sedimentation rates prevailing at both sites (>0.4 cm yr<sup>-1</sup>; Wei et al., 2021a). By studying these two high-resolution sedimentary records covering the Industrial Age (i.e., the period from 1888 to 2013 and from 1951 to 2013 AD in the proximal and distal cores, respectively; Figures 2c and 2d), we aim at unraveling the impacts of human perturbations of the PR watershed on terrestrial POC burial in the coastal ocean.

## 2. Materials and Methods

### 2.1. Site Description and Sample Collection

Two sediment cores were collected with a gravity corer aboard R/V Xintenglonghao in 2013 (Figure 1a). One core (113.72°E, 21.99°N, 21 m water depth, 1.24 m length, site WSB in Wei et al. (2020)) was retrieved close to the PR estuary (referred to from here on as the proximal core) and a second (distal) core (111.80°E, 21.40°N, 26.8 m water depth, 1.37 m length, site YJXB in Wei et al. (2020)) ~200 km to the southwest of the proximal

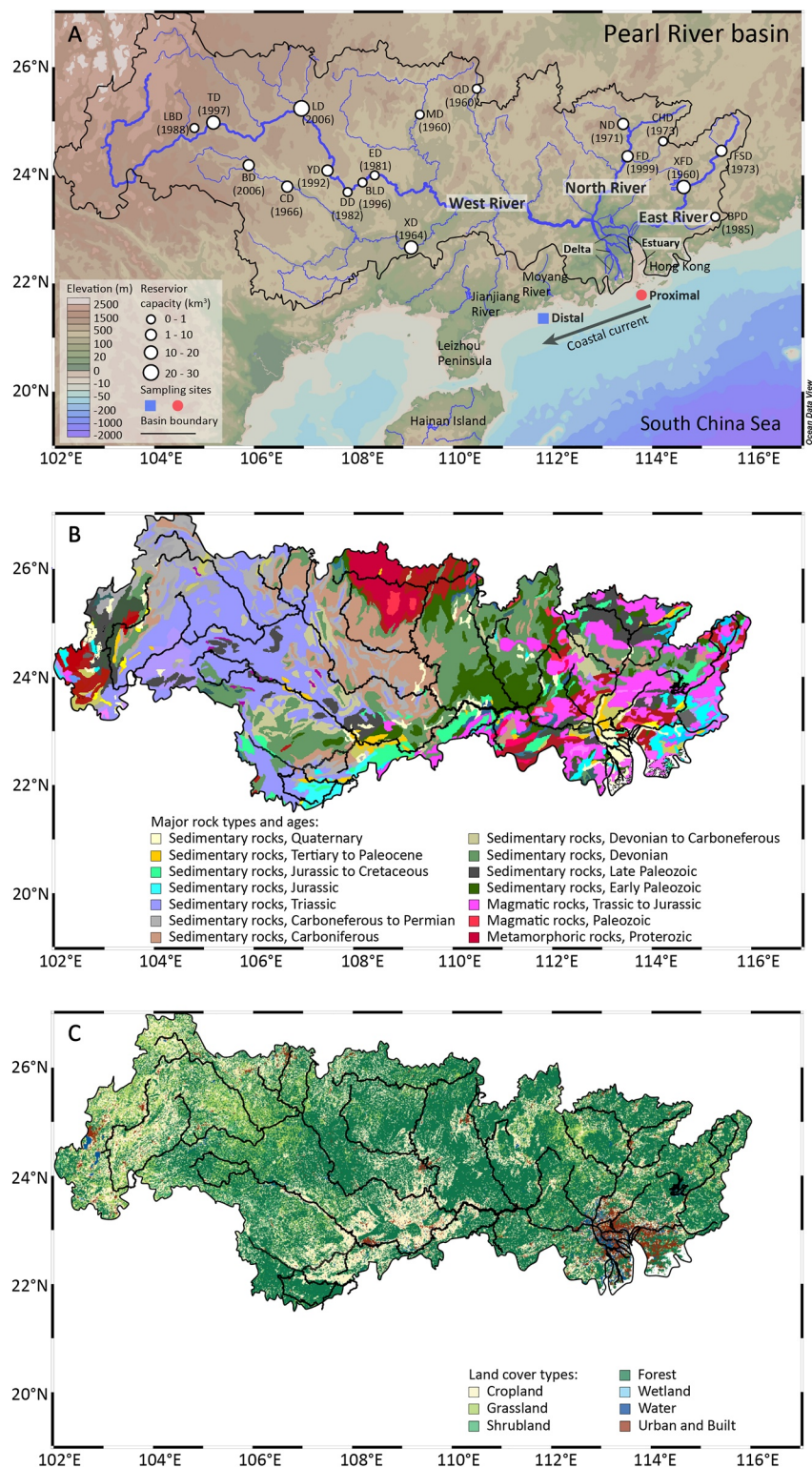


**Figure 1.** (a) Map of the Pearl River basin with locations of major reservoirs and sampling sites (proximal and distal cores), (b) geological map of the Pearl River basin (revised from Lin et al. (2019)), and (c) map showing different land cover classifications (from Globeland30, version 2020; [www.globeland30.org](http://www.globeland30.org); Chen et al., 2014). Black arrow in panel A represents the southwestward coastal current. In panel B, sedimentary, magmatic and metamorphic rocks are differentiated and colored according to age. Carbonates mainly occur in Triassic and Carboniferous formation, and black shales are found in late Paleozoic formations.

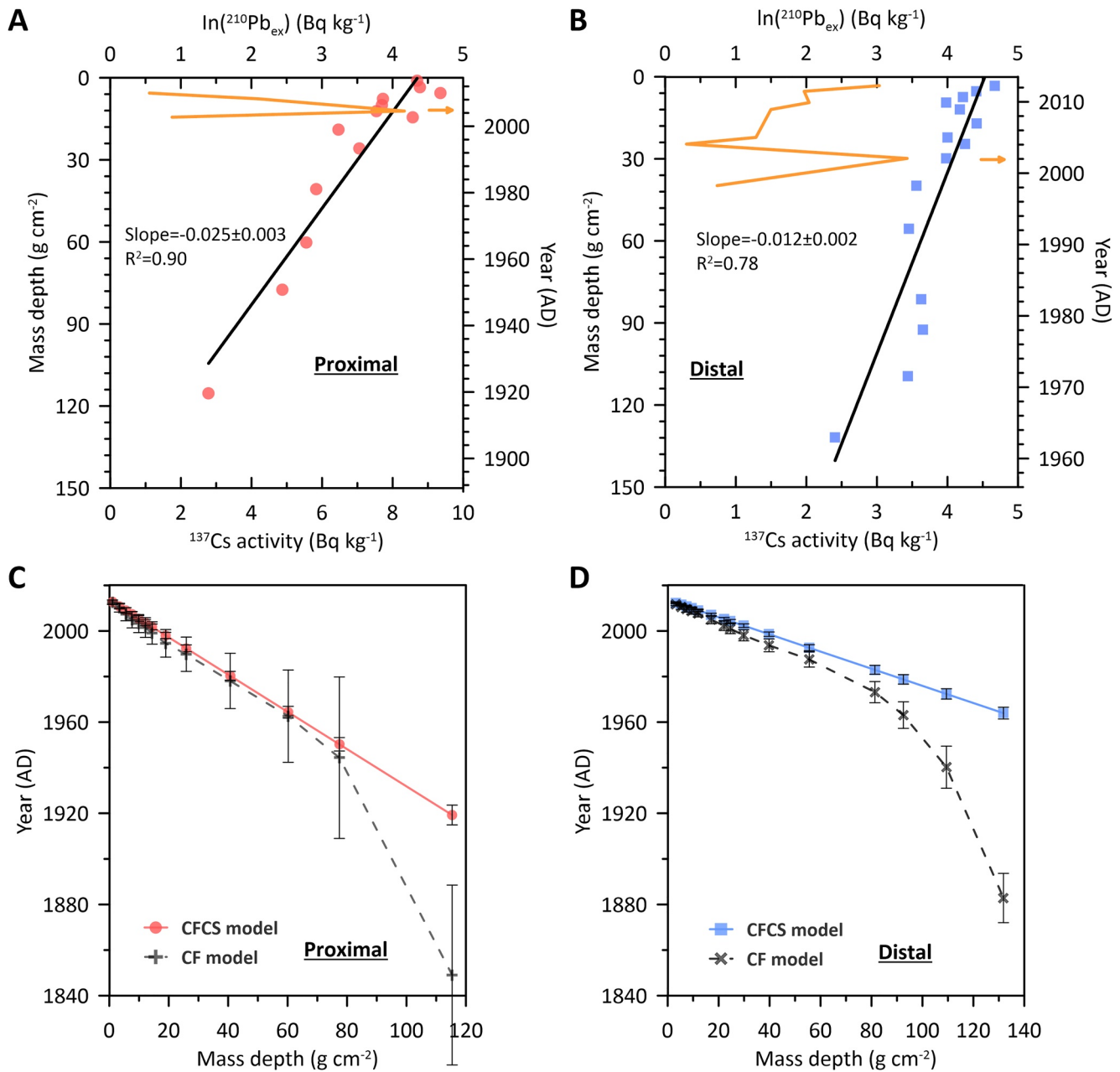


**Figure 2.** Activity-mass depth profiles of  $^{210}\text{Pb}_{\text{ex}}$  and  $^{137}\text{Cs}$  in the (a) proximal and (b) distal cores (yellow lines represent  $^{137}\text{Cs}$  activities, and yellow arrows indicate  $^{137}\text{Cs}$  peaks) and (c)–(d) the age comparison of CFCS and CF models in both cores.

core (Figure 1a). The two cores were split lengthwise and sectioned at 2 cm intervals. Aliquots of each sample were taken using syringes to measure dry bulk density, the remainders of each sample were transferred to pre-combusted aluminum envelopes, stored at  $-20^{\circ}\text{C}$  and later freeze-dried at  $-50^{\circ}\text{C}$  for further analyses.

## 2.2. Bulk Analyses

Grain size was measured via a Laser Particle Analyzer (LS230) following the sample pretreatment described by Z. Liu et al. (2005). Briefly, sediments were first pretreated with  $\text{H}_2\text{O}_2$  (10%) at  $50^{\circ}\text{C}$  and  $\text{HCl}$  (1 M) at  $60^{\circ}\text{C}$  for 24 hr followed by a series of distilled water rinsing steps to remove OC and biological shells, respectively. Sediments were then treated with  $\text{Na}_2\text{CO}_3$  (1 M) at  $85^{\circ}\text{C}$  for 4 hr to remove biogenic silica and neutralized to  $\text{pH} = 7$

by successive washing with distilled water. In addition, the dry bulk density of sediments was determined as a ratio of dry weight to syringe volume.

Dry samples weighing 10–15 g from selected intervals of both cores were sealed in plastic tubes for 20 days to ensure the secular equilibrium between  $^{210}\text{Pb}$  and  $^{214}\text{Pb}$ . Measurements of  $^{210}\text{Pb}$ ,  $^{137}\text{Cs}$ , and  $^{226}\text{Ra}$  activities were performed on a HPGe  $\gamma$  ray detector (GWL-120-15-LB-AWT, AMETEK, USA) for 24 hr, and excess  $^{210}\text{Pb}$  ( $^{210}\text{Pb}_{\text{ex}}$ ) activities were determined by subtracting the  $^{226}\text{Ra}$  activity from the total  $^{210}\text{Pb}$  activity (Sanchez-Cabeza & Ruiz-Fernández, 2012). The dry bulk density was used to calculate the cumulative weight of sediment (i.e., mass depth,  $\text{g cm}^{-2}$ ).

Prior to content,  $^{13}\text{C}$  and  $^{14}\text{C}$  analyses of bulk POC, carbonate was removed based on a modified acid pre-treatment method. Briefly, 6N HCl was added dropwise to the sediments in a silver boat, which was heated at  $60^\circ\text{C}$  for 1 hr to increase the acid reaction rate; these steps were repeated twice, and sediments were kept in an oven at  $60^\circ\text{C}$  overnight. OC content and  $^{13}\text{C}$  analyses were performed via a Vario EL Elemental Analyzer (EA) and a Finnigan MAT (DELTAplus XP) mass spectrometer interfaced with a Carlo Erba EA, respectively. The  $\delta^{13}\text{C}$  values are reported in ‰ relative to Vienna Pee Dee Belemnite (VPDB). The standard deviation of duplicate measurements ranged from 0.02 to 0.17‰ and averaged 0.09‰. Acidified samples for  $^{14}\text{C}$  analyses were combusted to gaseous  $\text{CO}_2$  by a Vario ISOTOPE EA, then reduced to graphite using an Ionplus AGE3 system (Wacker et al., 2010), and finally measured by an Ionplus MICADAS system at the Alfred Wegener Institute (Mollenhauer et al., 2021). Results are reported as  $\text{F}^{14}\text{C}$  and conventional  $^{14}\text{C}$  ages (yr BP) following conventions (Reimer et al., 2004). OC accumulation rate is calculated by multiplying OC content with mass accumulation rate (MAR).

### 2.3. Extraction, Quantification and Carbon Isotope Analyses of FAs

Methods for the extraction, purification and isolation of target FAs are similar to those described by Mollenhauer and Eglinton (2007) and Wei et al. (2021a). Dried and homogenized samples (70–140 g) were Soxhlet extracted with dichloromethane (DCM): methanol (MeOH) 9:1 (v/v) for 48 hr. After removal of the solvent by rotary evaporation, the total lipid extracts were saponified with 0.1 M potassium hydroxide (KOH) in MeOH:  $\text{H}_2\text{O}$  9:1 (v/v) at  $80^\circ\text{C}$  for 2 hr. The neutral fraction was liquid-liquid extracted into *n*-hexane, and the remaining solution was acidified to pH = 1 by adding Seralpure water and 12 N hydrochloric acid (HCl). The acid fraction was extracted into DCM, and FAs were subsequently converted to methyl ester derivatives (FAMES) by adding MeOH with known  $^{13}\text{C}$  and  $^{14}\text{C}$  compositions and 5% HCl under  $\text{N}_2$  atmosphere at  $50^\circ\text{C}$  overnight. After methylation, Seralpure water was added and FAMES were extracted into *n*-hexane. The FAMES were further separated by silica gel column chromatography and eluted with DCM: hexane 2:1 (v/v). About 5% of each FAME fraction was kept for compound-specific  $^{13}\text{C}$  analysis. The remaining 95% were separated on a gas chromatograph (GC, Agilent 6890N) equipped with a Restek Rxi-XLB capillary column (30 m, 0.53 mm, 0.5  $\mu\text{m}$ ) and a Gerstel preparative fraction collector (PFC) to obtain target compounds ( $\text{C}_{16}$ ,  $\text{C}_{18}$ ,  $\text{C}_{20}$ ,  $\text{C}_{22}$ ,  $\text{C}_{24}$ ,  $\text{C}_{26}$ ,  $\text{C}_{28}$ , and  $\text{C}_{30}$  FAMES).  $\text{C}_{20}$  and  $\text{C}_{22}$  as well as  $\text{C}_{28}$  and  $\text{C}_{30}$  FAMES were combined, respectively, to obtain sufficient sample size for  $^{14}\text{C}$  analysis.

The  $\delta^{13}\text{C}$  values of FAMES were determined in duplicate using a Finnigan MAT252 mass spectrometer connected to a Thermo Trace gas chromatograph via a combustion reactor. Standard mixtures of *n*-alkanes with known  $\delta^{13}\text{C}$  values were measured every six injections to determine the mean absolute deviation (i.e., accuracy) of 0.2‰. The reproducibility for duplicate measurements of each FA ranged from <0.1‰ to 0.5‰. The  $^{14}\text{C}$  analyses of FAMES were performed on a MICADAS system (Fahrni et al., 2013; Ruff et al., 2010; Synal et al., 2007) coupled with a vario ISOTOPE EA via a gas interface system. The FAME  $\text{F}^{14}\text{C}$  values were corrected for procedural blanks ( $1.375 \pm 0.140 \mu\text{g C}$ ,  $\text{F}^{14}\text{C}$ :  $0.541 \pm 0.052$ ) determined by processing standard materials alongside the samples according to the method of Sun et al. (2020). The  $\delta^{13}\text{C}$  and  $\text{F}^{14}\text{C}$  values of FAMES were corrected for the derivative methyl carbon added during methylation and uncertainties were error-propagated.

### 2.4. Source Apportionment Calculations

A dual-carbon isotope ( $\delta^{13}\text{C}$  and  $\text{F}^{14}\text{C}$ ) model was used to quantify the fractional OC contributions from marine ( $f_M$ ), terrestrial biospheric ( $f_{\text{TB}}$ ) and petrogenic ( $f_P$ ) sources to sediments of the two cores as follows:

$$\delta^{13}\text{C}_M \times f_M + \delta^{13}\text{C}_{\text{TB}} \times f_{\text{TB}} + \delta^{13}\text{C}_P \times f_P = \delta^{13}\text{C}_{\text{OC}} \quad (1)$$

$$F^{14}C_M \times f_M + F^{14}C_{TB} \times f_{TB} + F^{14}C_P \times f_P = F^{14}C_{OC} \quad (2)$$

$$f_M + f_{TB} + f_P = 1 \quad (3)$$

where the  $F^{14}C$  value of petrogenic POC ( $F^{14}C_p$ ) is assumed to be 0 (“ $^{14}C$ -free”), and its  $\delta^{13}C$  value ( $\delta^{13}C_p$ ) is determined from rock samples collected in the PR basin ( $-24.8 \pm 1.8\%$ ,  $n = 133$ ; data from Cui et al., 2017; Lin et al., 2019) representing bedrock-derived petrogenic POC or from coal fly ash from northern China (i.e., the main source region of coal i.e., used in the power plants in the Pearl River basin,  $-23.4 \pm 3.7\%$ ,  $n = 3$ ; data from Li et al., 2021; Liu et al., 2020) indicative of fly ash-derived petrogenic POC. For  $\delta^{13}C$  and  $F^{14}C$  values of marine POC ( $\delta^{13}C_M$  and  $F^{14}C_M$ ), the Suess effect needs to be considered. Due to substantial anthropogenic emissions of  $^{13}C$ -depleted  $CO_2$  to the atmosphere (Druffel & Benavides, 1986), the  $\delta^{13}C$  value of atmospheric  $CO_2$  decreased by ca. 0.16‰ during 1900–1950 and by about 1‰ since 1950 (Graven et al., 2017). However, the Suess effect on the  $\delta^{13}C$  value of marine POC is difficult to quantify due to the complexity of marine physical and biogeochemical processes. Thus, we selected a value of  $-21 \pm 1\%$  to represent  $\delta^{13}C_M$  based on phytoplankton (Chen et al., 2008; He et al., 2010) and suspended particulate matter (Blattmann et al., 2018a, 2018b) data in the SCS, with  $\pm 1\%$  uncertainty accounting for the potential changes in  $\delta^{13}C_M$  over the last century. The  $F^{14}C$  value of atmospheric  $CO_2$  has been impacted by nuclear weapon testing in the late 1950s and early 1960s, which led to a doubling of the  $^{14}C$  amount in the atmosphere (Graven et al., 2017) and excess  $^{14}C$  in the surface ocean, due to limited air-sea exchange with a delay of 5–10 yr (Schuur et al., 2016). As direct time-series measurements of  $^{14}C$  of the regional seawater dissolved inorganic carbon (DIC) are not available, a coral  $^{14}C$  record of seawater DIC in the SCS (Mitsuguchi et al., 2007) is used here to constrain the  $F^{14}C_M$  endmember. However, the record only covers a period from 1950 to 2000. For the sediment deposited before 1950, we assumed  $F^{14}C_M$  to be  $0.96 \pm 0.01$ , because it remained fairly stable at  $0.96 \pm 0.01$  between 1950 and 1960 (prior to peak nuclear weapons testing) in the coral record (Figure S3 in Supporting Information S1, Mitsuguchi et al., 2007). For sediments deposited after 2000,  $F^{14}C_M$  values were obtained from linear regression (a slope of  $0.003 \text{ yr}^{-1}$ ) of  $F^{14}C$  values between the coral record (1990–2000) and the surface DIC measured directly in the SCS between 2014 and 2016 (Figure S3 in Supporting Information S1; Ding et al., 2020; Gao et al., 2019).  $F^{14}C_{28+30FAs}$  and  $\delta^{13}C_{28+30FAs}$  values are employed to define  $\delta^{13}C$  and  $F^{14}C$  values of terrestrial biospheric POC ( $F^{14}C_{TB}$  and  $\delta^{13}C_{TB}$ ; detailed source assignments of FAs are provided in the Text S1 in Supporting Information S1), respectively, with a  $^{13}C$  fractionation factor ( $\delta^{13}C_{biomass} - \delta^{13}C_{FA}$ ) of 4–7‰ proven to be applicable in the China marginal seas (Tao et al., 2016; Wei et al., 2021a). However, the chosen fractionation range (4–7‰) sometimes returns implausible  $f_M$  or  $f_P$  ( $< 0$ ) when applied in our model. Thus, a plausible fractionation was determined first by a matrix of calculations for every sediment interval (Figure S4 in Supporting Information S1). As  $F^{14}C_{28+30FAs}$  values are only measured in a few intervals, we use linear interpolation of  $F^{14}C_{28+30FAs}$  values for the unmeasured intervals. Minor decay corrections were applied to all reported  $F^{14}C$  values following the equation:

$$F^{14}C_y = F^{14}C \times \exp((1950 - y)/8267) \quad (4)$$

where  $y$  is the time of deposition and  $F^{14}C_y$  is the coral-based  $F^{14}C$  value of DIC at the time of deposition (Reimer et al., 2004; Soulet et al., 2016; Stuiver & Polach, 1977). To account for the natural end-member variability, we ran a Bayesian Markov chain Monte Carlo framework using Matlab (R2015a, MathWorks, USA) to estimate the resulting uncertainties in the calculated OC fractions/pools (Bosch et al., 2015). Briefly, individual end-member values are assumed to be normally distributed and 1,000,000 out of 100,000,000 random samples from the normal distribution of each end-member within the given mean and standard deviations were taken to simultaneously fulfill the given system in simulations. The mean relative contributions and the standard deviation of different OC sources were then estimated (Bosch et al., 2015).

### 3. Results

#### 3.1. Sediment Chronology

Both the Constant Flux Constant Sedimentation model (CFCS) and the Constant Flux model (CF) were tested to generate age models of the two cores (for detailed description of the CFCS and CF models we refer to Sanchez-Cabeza and Ruiz-Fernández (2012)). The assumption of constant flux and constant sedimentation underlying the CFCS model approach is not fully met in our cores. On the other hand, the CF model-derived ages can only ideally be obtained in cases where the complete  $^{210}Pb_{ex}$  inventory of the sediment column is known. In

all other cases, ages are highly sensitive to the value assumed for inventory below the lowermost sediment layer measured for radionuclide activities (Sanchez-Cabeza & Ruiz-Fernández, 2012). Both the proximal and distal cores were too short to allow for the  $^{210}\text{Pb}_{\text{ex}}$  to reach background values (i.e., a depth in which  $^{210}\text{Pb}_{\text{ex}} = 0$ ), a requirement for the determination of the full  $^{210}\text{Pb}_{\text{ex}}$  inventory (Figures 2a and 2b). In contrast to other coastal cores in which significant changes in clay fraction (0%–40%) have been reported to correlate with  $^{210}\text{Pb}_{\text{ex}}$  (e.g., Sun et al., 2017), the clay fraction in our cores varied only within a small range (7%–15%) and was not directly correlated with  $^{210}\text{Pb}_{\text{ex}}$  ( $r = 0.28$ ,  $p = 0.15$ , Figure S1 in Supporting Information S1). Thus,  $^{210}\text{Pb}_{\text{ex}}$  are not normalized to grain size. For the CFCS model, apparent mass accumulation rates (MAR) were calculated based on the following equation:

$$\text{MAR} = -\lambda/\text{slope} \quad (5)$$

where  $\lambda$  is the decay constant of  $0.03118 \text{ yr}^{-1}$  and the slope is taken from the plot of  $\ln(^{210}\text{Pb}_{\text{ex}})$  against mass depth (Figures 2a and 2b).

The age estimates obtained from the two models agree very well (with on average 2.0 and 2.6 yr difference, Figures 2c and 2d) in the upper and middle layers of the two cores but a larger discrepancy was observed in the bottom layer, mainly due to the missing  $^{210}\text{Pb}_{\text{ex}}$  inventory. We consider this effect to be stronger than the bias introduced by sedimentological changes. We therefore selected the CFCS model to derive the age models; moreover, the focus of our study is on the upper part of the records, where the results of the two models showed good agreement and sediment properties also matched well between the two cores when using the age models based on the CFCS model (Figures 2a–2d). Similar studies in this coastal ocean have implied relatively stable sedimentation rates over the last century, evidenced by strong linear correlations between the logarithm of  $^{210}\text{Pb}_{\text{ex}}$  and mass depths (e.g., Hu et al., 2008; Jia et al., 2013). The MAR were calculated to be  $1.22 \pm 0.12 \text{ g cm}^{-2} \text{ yr}^{-1}$  at the proximal site and  $2.66 \pm 0.40 \text{ g cm}^{-2} \text{ yr}^{-1}$  at the distal site (Figures 2a and 2b). It was not possible to derive additional age constraints from  $^{137}\text{Cs}$ , which was often near or below the detector limit. However, a possible simultaneous spike is seen in the upper part of both cores irrespective of model chosen (Figures 2a and 2b). This delayed spike - usually expected around 1963 AD - can have various causes (mineralogy, porosity, and delayed riverine supply). The age uncertainty increased downcore from 0.9 to 6.3 yr (average 3.3 yr) and from 0.5–4.0 yr (average 2.0 yr) in the proximal and distal cores, respectively (Figures 2c and 2d). However, after the 1970s, the age uncertainty was less than 2.8 and 2.4 yr in both cores (Figures 2c and 2d), that is, these small age uncertainties have little effect on the placement of time makers in the upper part of the records in the following discussion.

### 3.2. Bulk Sedimentary Characteristics

The mean grain size ranged from 14 to 87  $\mu\text{m}$  in the proximal core during 1890–2013, which was comparable to that (19–86  $\mu\text{m}$ ) in the distal core during 1974–2013, but much finer than that (34–170  $\mu\text{m}$ ) during 1950–1974 (Figure 3a). Both sediment cores show an increase of fine (i.e., clay and silt) and decrease of coarse (i.e., fine sand) sediment accumulation over time (Figures 3b and 3c). POC accumulation rate remained at  $\sim 6 \text{ mg cm}^{-2} \text{ yr}^{-1}$  before the 1950s, but increased up to  $10.5 \text{ mg cm}^{-2} \text{ yr}^{-1}$  at the top of the proximal core (Figure 3d), being negatively correlated with mean grain size ( $r = -0.55$ ,  $p < 0.001$ ). In the distal core, POC accumulation rate displayed a general increase from 5.8 to  $22.1 \text{ mg cm}^{-2} \text{ yr}^{-1}$  since 1950 (Figure 3d), showing a similar negative correlation with mean grain size ( $r = -0.65$ ,  $p < 0.001$ ).

In addition to changes in OC accumulation rate,  $\delta^{13}\text{C}$  and  $\text{F}^{14}\text{C}$  values of POC ( $\delta^{13}\text{C}_{\text{OC}}$  and  $\text{F}^{14}\text{C}_{\text{OC}}$ ) also changed through time at both sites (Figures 3e and 3g). The  $\delta^{13}\text{C}_{\text{OC}}$  values in the proximal core remained stable at  $-24.8 \pm 0.1\text{‰}$  between 1890 and 1928 and  $-23.3 \pm 0.1\text{‰}$  between 1954 and 1974, followed by an increase of ca. 1.5 and 1‰, respectively, after each period (Figure 3e). In comparison,  $\delta^{13}\text{C}_{\text{OC}}$  values in the distal core were  $\sim 1\text{‰}$  lower compared to the proximal core between 1952 and 1974 but similar to the  $\delta^{13}\text{C}_{\text{OC}}$  values in the proximal core after  $\sim 1974$ , except for a high value of  $-22.3 \pm 0.1\text{‰}$  in  $\sim 1980$  (Figure 3e).  $\text{F}^{14}\text{C}_{\text{OC}}$  values increased in line with  $\delta^{13}\text{C}_{\text{OC}}$  values ( $r = 0.93$ ,  $p < 0.01$ ) at both sites, from  $0.657 \pm 0.004$  ( $3,380 \pm 50$  yr BP, conventional radiocarbon age) at the bottom to  $0.757 \pm 0.003$  ( $2,240 \pm 50$  yr BP) at the top in the proximal core, and from  $0.512 \pm 0.004$  ( $5,370 \pm 60$  yr BP) to  $0.794 \pm 0.004$  ( $1,850 \pm 40$  yr BP) in the distal core (Figure 3g). POC in the distal core was also significantly older compared to the proximal core before  $\sim 1974$  (Figure 3g).

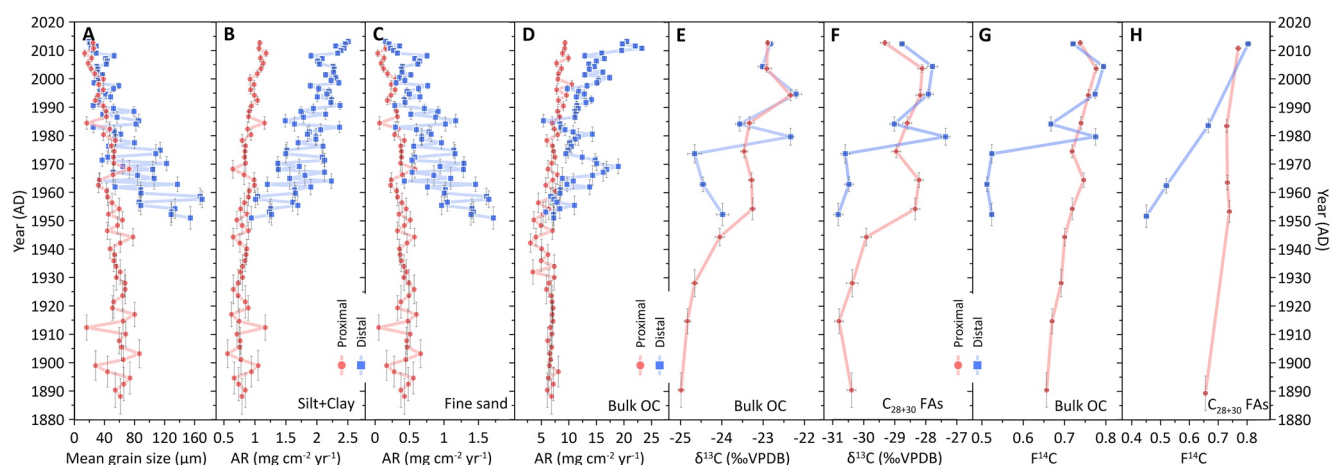


**Figure 3.** Temporal variations in (a) mean grain size, accumulation rates of (b) the fine fraction (silt and clay), (c) coarse fraction (fine sand) and (d) OC ( $AR_{OC}$ ), which are correlated with mean grain size, correlation coefficient ( $r$ ) of  $-0.55$  ( $p < 0.001$ ) in the proximal core and  $-0.65$  ( $p < 0.001$ ) in the distal core,  $\delta^{13}C$  values of (e) bulk OC and (f)  $C_{28+30}$  FAs, and  $F^{14}C$  values of (g) bulk OC and (h)  $C_{28+30}$  FAs. Pearson correlation analyses were performed using SPSS 19.

### 3.3. Changes in FA Abundances and Carbon Isotopes

Saturated FAs ( $C_{14}$  to  $C_{32}$ ) in the two cores exhibited a bimodal distribution with an even-carbon-number predominance, that is,  $C_{max}$  at  $C_{16}$  among short-chain homologs and  $C_{24}/C_{26}$  among the long-chain counterparts (Figures S2a and S2b in Supporting Information S1). The short-chain (e.g.,  $C_{16+18}$ ) FA abundances significantly decreased downcore, but those of long-chain (e.g.,  $C_{28+30}$ ) FAs remained relatively comparable throughout the whole core (Figures S2c and S2d, Table S1 in Supporting Information S1). The  $\delta^{13}C$  values of short-chain FAs (i.e.,  $C_{16}$  and  $C_{18}$ ) ranged from  $-29.6 \pm 0.2$  to  $-25.7 \pm 0.2\text{‰}$  and from  $-30.1 \pm 0.2$  to  $-27.7 \pm 0.2\text{‰}$  in the proximal and distal cores, respectively, and are slightly higher than those of long-chain FAs (i.e.,  $C_{24}$ ,  $C_{26}$ ,  $C_{28}$ , and  $C_{30}$ ) in each interval (proximal:  $-31.2 \pm 0.2$  to  $-26.8 \pm 0.2\text{‰}$ , distal:  $-31.4 \pm 0.2$  to  $-26.2 \pm 0.2\text{‰}$ ; Figure S2f, S2g, and Table S2 in Supporting Information S1). Among these FAs,  $\delta^{13}C$  of  $C_{28+30}$  FAs (weighted average,  $\delta^{13}C_{28+30FAs}$ ) values remained low at  $-30.8 \pm 0.1$  to  $-29.9 \pm 0.1\text{‰}$  before the 1950s and since then increased substantially to  $-28.1 \pm 0.1\text{‰}$  at the top of the proximal core (Figure 3f). At the distal site,  $\delta^{13}C_{28+30FAs}$  values remained constant at  $-30.8 \pm 0.2$  to  $-30.5 \pm 0.1\text{‰}$  before  $\sim 1974$  and then significantly increased to  $-29.0 \pm 0.1$  to  $-27.4 \pm 0.1\text{‰}$  after  $\sim 1974$  (Figure 3f).  $F^{14}C$  values of  $C_{16}$  and  $C_{18}$  FAs generally changed from  $0.835 \pm 0.009$  to  $1.021 \pm 0.009$  and from  $0.753 \pm 0.010$  to  $1.050 \pm 0.010$  in the proximal and distal cores, respectively, and were also higher than those of  $C_{24}$ ,  $C_{26}$  and  $C_{28+30}$  homologs (proximal:  $0.578 \pm 0.006$  to  $0.790 \pm 0.011$ , distal:  $0.430 \pm 0.006$  to  $0.886 \pm 0.009$ ) in each interval, except the  $C_{16}$  FA from the depth of the distal core that was deposited  $\sim 1984$  and displayed an unusually low  $F^{14}C$  value of  $0.571 \pm 0.006$  (Figures S2h, S2i, Table S4 in Supporting Information S1).  $F^{14}C$  values of  $C_{28}$  and  $C_{30}$  FAs ( $F^{14}C_{28+30FAs}$ ) were  $0.732 \pm 0.007$  to  $0.769 \pm 0.009$  ( $2,110 \pm 90$  to  $2,530 \pm 90$  yr BP) after  $\sim 1950$ , which were somewhat higher than that at the proximal core bottom ( $0.656 \pm 0.006$ ,  $3,390 \pm 70$  yr BP, Figure 3h). At the distal site,  $F^{14}C_{28+30FAs}$  values ( $0.665 \pm 0.008$  and  $0.804 \pm 0.009$ ) were similar to the values determined at the proximal site after  $\sim 1974$ , but they ( $0.451 \pm 0.009$  and  $0.520 \pm 0.009$ ) were more depleted relative to those at the proximal site before  $\sim 1974$  (Figure 3h). The sources of FAs with different chain lengths are discussed in more detail in the Text S1 in Supporting Information S1.

## 4. Discussion

### 4.1. Temporal Variations in Sediment Grain Size and Accumulation

Both sediment cores display an increase of fine (i.e., clay and silt) and decrease of coarse (i.e., fine sand) sediment accumulation over time (Figures 3b and 3c). The PR-derived mineral particles have a unimodal grain-size distribution with a median value of 2–9  $\mu m$  in the wet season and 6–35  $\mu m$  in the dry season (Dong et al., 2006). The corresponding mean mineral particle flux, calculated based on eight hydrological stations located upstream of the PR delta, was  $\sim 80$ – $85$   $Tg\ yr^{-1}$  during the 1950s–1980s and decreased to  $40$   $Tg\ yr^{-1}$  in the 2000s (Figure 5f) as a result of damming (Dai et al., 2008). The proximal site should directly reflect the grain size changes of the

PR-derived mineral particles due to its proximity to the river mouth, and record decreasing mineral particle flux from the PR, in spite of the increased fine sediment fluxes (Figure 3b). However, mineral particle fluxes recorded upstream of the PR delta are not representative of the total PR mineral particle flux discharged into the estuary since intensive human activities in the delta (e.g., agriculture, deforestation, urbanization, industrialization, and embankment) and sedimentological effects occurring in the extensive lowland water network are not accounted for. This lack of monitoring may explain the apparent discrepancy between the decreased mineral particle flux upstream since the 1980s and the increased fine sediment accumulation at the proximal site since the 1970s.

By comparison, sediments deposited at the distal site were much coarser than at the proximal site before ~1974 (Figure 3a). This pattern cannot be explained by hydrodynamic sorting during transport from the river mouth to the distal site, which would be expected to result in preferential transport of fine rather than coarse sediment along the net transport pathways (McLaren, 1985). Sediment winnowing at the distal site before ~1974 can also be excluded, due to the overall higher accumulation rates of total and fine sediments at that site in comparison to the proximal site (Figures 3b and 3c) and the  $^{210}\text{Pb}$  and  $^{14}\text{C}$  age constraints (marine  $\text{C}_{16}$  and  $\text{C}_{18}$  FAs contain bomb- $^{14}\text{C}$ ; Figures S2g and S2h in Supporting Information S1). The higher accumulation rate of total and fine sediments at the distal site could be attributed to a transport mechanism described as “storing in summer and transport in winter,” for example, the PR-derived mineral particles are deposited first at the proximal site in summer and then re-transferred to the distal region by the strong coastal current in winter (Ge et al., 2014). In contrast, the coarse sediment fraction deposited at the distal site before ~1974 may originate from other source areas via lateral transport. Indeed, we consider seabed reworking the main mechanism responsible for the delivery of coarse sediments. However, rather than supply from the adjacent Moyang River and flood or storm-related inputs, we attribute this input to the ancient PR delta on the southwestern shelf off the modern PR estuary, which consists of relict littoral, bioclast-bearing and fine or medium-fine sands deposited before 6,000 cal. yr BP (Li & Li, 2017; Yim et al., 2006). In contrast, the fine grain size (mean diameter of 8–13  $\mu\text{m}$ ) and low flux (0.8  $\text{Tg yr}^{-1}$ ) of Moyang-derived mineral particles (Gao et al., 2015) cannot explain an additional accumulation of up to 1.2  $\text{g cm}^{-2} \text{yr}^{-1}$  of coarse sediment at the distal site (Figure 3c), 50 km from the Moyang River mouth. Likewise, enhanced coastal erosion with successive regional sea-level rise (Cai et al., 2009) and more frequent (and particularly strong) storm events since the 1970s (Mei & Xie, 2016) should enhance winnowing at both sites, contrary to the observed increased accumulation of fine sediments at the distal site only (Figure 3c). In conclusion, the progressively smaller grain-size difference between the two sites since ~1974 (Figure 3a) reflects a strongly increased burial of PR-derived fine mineral particles in the coastal ocean since then.

## 4.2. Temporal Variations in OC Quantity and Quality in the Coastal South China Sea

### 4.2.1. Changes in OC Accumulation and Composition Shown by Bulk $^{13}\text{C}$ and $^{14}\text{C}$ Isotopes

Our data reveal profound changes in the POC burial fluxes off the PR during the Industrial Age. POC accumulation rates remained low at ~6  $\text{mg cm}^{-2} \text{yr}^{-1}$  before the 1950s but then increased by 70% to the present at the proximal site (Figure 3d). A similar but more pronounced increase in POC burial occurred at the distal site since the 1950s (Figure 3d). The concurrent decrease in grain size may explain the increased POC burial due to their negative correlations at both sites ( $r_{[\text{Proximal}]} = -0.55$ ,  $r_{[\text{Distal}]} = -0.65$ , both  $p < 0.001$ ; Figures 3a and 3d), likely reflecting higher loadings (Lin et al., 2019) and better preservation of POC on fine mineral particles (Blair & Aller, 2012). In addition to quantitative changes in POC burial, the POC composition also changed at both sites, as shown by the bulk  $^{13}\text{C}$  and  $^{14}\text{C}$  isotope variations (Figures 3e and 3g). The observed convergence of  $\delta^{13}\text{C}_{\text{OC}}$  and  $F^{14}\text{C}_{\text{OC}}$  values at both sites after 1974 is consistent with a decreased supply/influence of reworked POC at the distal site evident in the grain size data, and dominance of PR-derived POC burial at both sites. The overall  $\delta^{13}\text{C}_{\text{OC}}$  and  $F^{14}\text{C}_{\text{OC}}$  trends are toward higher values and can be caused by various factors: increased marine POC production relative to terrestrial POC input (Blattmann et al., 2018a, 2018b; Jia et al., 2013), preferential degradation of fresh/marine POC during burial (Wei et al., 2020), increased fresh/young  $\text{C}_4$  plant input (Cerling et al., 1997; Goñi et al., 1997), increased incorporation of bomb- $^{14}\text{C}$ , increased POC from riverine primary production caused by massive anthropogenic input of inorganic nutrients (Jia et al., 2013), or a shift toward erosion of lowland POC through damming (Yang et al., 2019). Burial of POC from riverine primary production is negligible at both sites due to its rapid degradation within the PR estuary as demonstrated elsewhere (Wei et al., 2020). The other potential factors explaining the increasing  $\delta^{13}\text{C}_{\text{OC}}$  and  $F^{14}\text{C}_{\text{OC}}$  values cannot be deconvolved at the bulk-level, but can be elucidated by means of  $^{13}\text{C}$  and  $^{14}\text{C}$  analyses of biomolecular tracers unique to the epicuticular wax cover of terrestrial vascular plants (Eglinton et al., 2021; Kusch et al., 2021a, 2021b; Wei et al., 2021a).

#### 4.2.2. Further Elucidation of OC Compositional Changes Based on the $^{13}\text{C}$ and $^{14}\text{C}$ Isotope Composition of $\text{C}_{28+30}$ FAs

$\text{C}_{28+30}$  FAs can be transiently stored in soils within river basins for hundreds to thousands of years, resulting in old  $^{14}\text{C}_{28+30\text{FAs}}$  ages in marine surface sediments (Kusch et al., 2021a, 2021b). Pre-aged  $\text{C}_{28+30}$  FAs also originate from a continuum of different terrestrial biospheric POC sub-pools that have been operationally defined as fast-cycling (<100 yrs) and slow-cycling (200 to >50,000 yr) pools (French et al., 2018; Vonk et al., 2019). Their relative contributions vary with time due to environmental/ecosystem changes in the river catchment, which may be negligible on decadal timescales but could be significant over longer time-scales (e.g., the Holocene) or in strongly anthropogenically altered catchments (Kusch et al., 2021a, 2021b). Accumulating evidence highlights that lowlands can store, alter and recycle POC exported by rivers (Repasch et al., 2021; Shen et al., 2021; Torres et al., 2017), contributing disproportionately to the terrestrial biospheric POC export to the coastal ocean (Eglinton et al., 2021; Galy et al., 2011; Hemingway et al., 2016). Thus, the isotope shifts of  $\text{C}_{28+30}$  FAs (weighted average) in our two sediment cores mirror the changes in relative contributions of different terrestrial biospheric POC sub-pools and can reflect the ecosystem changes in the PR lowland areas with strong anthropogenic perturbations since the 1890s. Furthermore, we can exclude diagenetic and mineralogical biases on  $\text{F}^{14}\text{C}_{28+30\text{FAs}}$  values. In contrast to the sharp downcore decrease of short-chain (e.g.,  $\text{C}_{16+18}$ ) FA abundances,  $\text{C}_{28+30}$  FA abundances remained comparable over time in both cores (Figures S2c and S2d in Supporting Information S1), suggesting low degradation of  $\text{C}_{28+30}$  FAs after burial and absence of selective degradation that could influence the isotope composition (Mollenhauer & Eglinton, 2007). Likewise, grain-size effects on  $\text{F}^{14}\text{C}_{28+30\text{FAs}}$  can be excluded. Grain size would affect  $\text{F}^{14}\text{C}$  values of bulk POC and FAs in different ways: coarse mineral particles exported from rivers contain older particulate POC than fine mineral particles due to increased contribution of very old POC from bedrock-derived detrital particles (Yu et al., 2019); however,  $\text{C}_{28+30}$  or other long-chain FAs in river-derived coarse mineral particles are younger than those in fine particles, as coarse mineral particles contain fresh plant fragments (young FAs) but FAs in fine mineral particles have resided in soils for hundreds-to-thousands of years before export to rivers (Bao et al., 2016; Wei et al., 2021a; Yu et al., 2019). In the coastal ocean, fine mineral particles will stabilize OC during lateral transport and result in increased ages of POC and FAs relative to coarse mineral particles (Wei et al., 2020, 2021a). If grain-size effects controlled  $^{14}\text{C}$  values of POC and FAs, we would expect increased  $\text{F}^{14}\text{C}_{\text{OC}}$  values and decreased  $\text{F}^{14}\text{C}_{28+30\text{FAs}}$  values due to the fining of mineral particles since the 1970s, instead we observe the opposite changes of  $\text{F}^{14}\text{C}_{28+30\text{FAs}}$  values with grain size in both sediment cores (Figure 4d), which can be explained by reduced lateral supply of relict sands to the distal site. In addition, grain size has relatively minor effects on the  $\delta^{13}\text{C}$  values of POC and FAs (Yu et al., 2019), and the fining of mineral particles cannot explain the enrichment of  $\delta^{13}\text{C}_{\text{OC}}$  and  $\delta^{13}\text{C}_{28+30\text{FAs}}$  values toward the core-top (Figure 4c). Thus, we consider grain size, other than the lateral supply of relict sands to the distal core, to have minor effects on temporal isotope changes of POC and FAs in the two cores.

At the proximal site,  $\delta^{13}\text{C}_{28+30\text{FAs}}$  values increased substantially since the 1950s and  $\text{F}^{14}\text{C}_{28+30\text{FAs}}$  values were somewhat higher after ~1950 ( $0.732 \pm 0.007$  to  $0.769 \pm 0.009$ ,  $2,110 \pm 90$  to  $2,530 \pm 90$  yr BP) than before (core bottom;  $0.656 \pm 0.006$ ,  $3,390 \pm 70$  yr BP, Figure 3f). Since  $\text{C}_{28+30}$  FA abundances at the proximal site were comparable or slightly lower after 1950 (Figures S2c and S2d in Supporting Information S1), the observed  $\delta^{13}\text{C}_{28+30\text{FAs}}$  and  $\text{F}^{14}\text{C}_{28+30\text{FAs}}$  trends reflect a qualitative shift toward either increased proportions of fresh and  $^{13}\text{C}$ -enriched biospheric POC (i.e.,  $\text{C}_4$  plants containing some proportion of bomb- $^{14}\text{C}$ ) and/or decreased proportions of “older” and  $^{13}\text{C}$ -depleted biospheric POC since the 1950s. Similar observations have been made in earlier studies from the same region where higher  $\text{C}_4$  plant-derived POC export was invoked on the basis of increased  $\delta^{13}\text{C}$  values of leaf wax-derived  $\text{C}_{29}$  and  $\text{C}_{31}$  alkanes deposited in the 1930s and since the 1970s (Xu et al., 2016), and increased bulk POC  $\delta^{13}\text{C}$  values in conjunction with C/N ratio and lignin phenol data (Li et al., 2017). At the distal site,  $\delta^{13}\text{C}_{28+30\text{FAs}}$  and  $\text{F}^{14}\text{C}_{28+30\text{FAs}}$  values were similar to the values determined at the proximal site after ~1974, but they were more depleted than those at the proximal site before ~1974 (Figures 3f and 3h). This contrast reveals a suddenly increased impact of vegetation changes in the PR basin on the sedimentary  $\text{C}_{28+30}$  FA isotope composition that outweighs the signal from deposition of reworked  $\text{C}_{28+30}$  FAs after ~1974. This transition is also evident in the progressive decrease in mean grain size (Figure 3a) and the elevated abundances of  $\text{C}_{28+30}$  FAs after ~1974 at the distal site (Figure S2d in Supporting Information S1). Reworked  $\text{C}_{28+30}$  FAs and OC associated with coarser mineral particles (Figure 4d) in the lower layers of the distal core likely originated from relict seabed sediments containing aged biospheric and petrogenic POC. Thus, PR-derived finer mineral particles carrying fresh and  $^{13}\text{C}$ -enriched POC with stronger  $\text{C}_4$ -plant signals became a major contribution to the distal site only

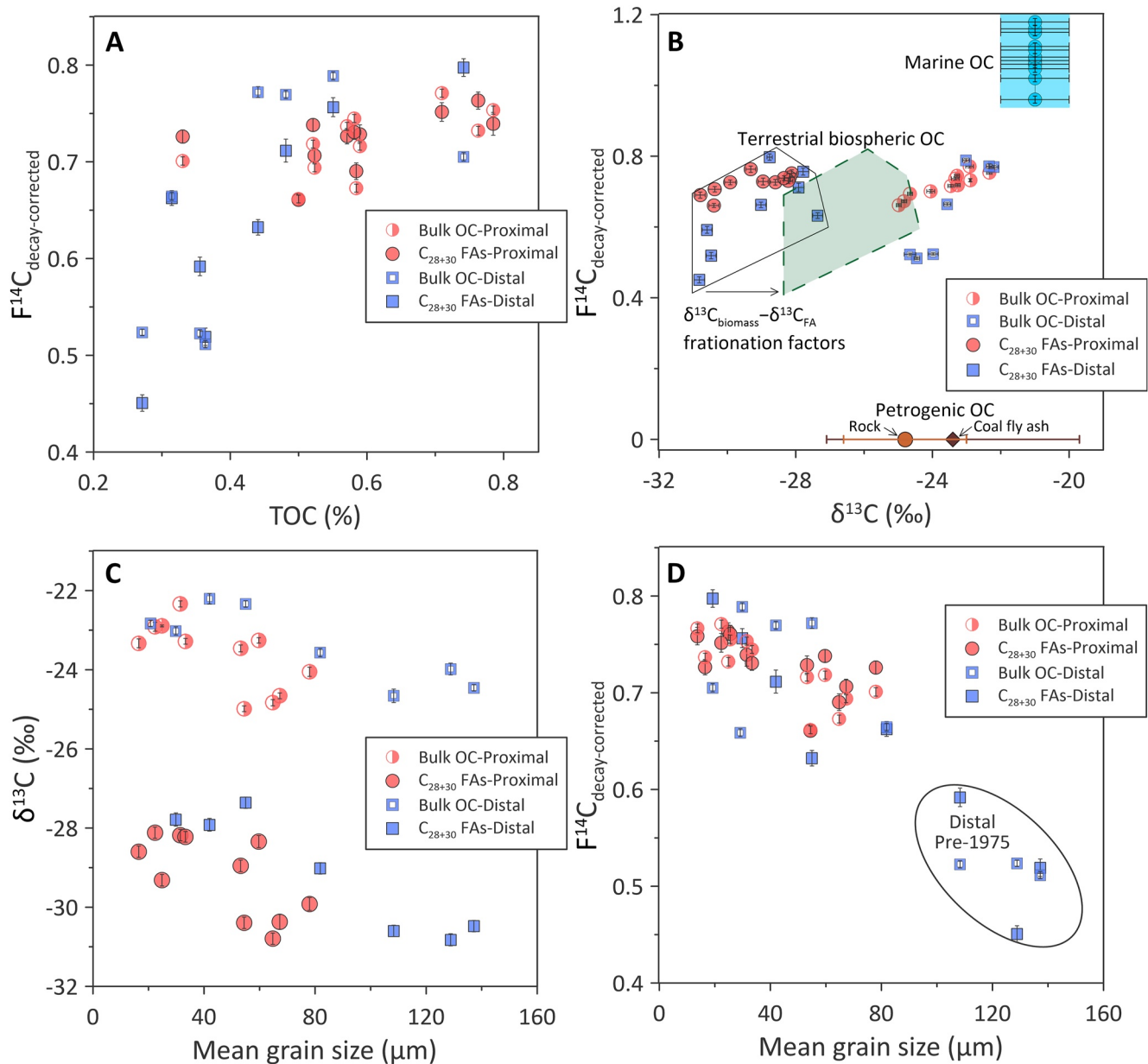


**Figure 4.** (a) Cross plot of decay-corrected F<sup>14</sup>C of bulk OC and C<sub>28+30</sub> FAs as a function of TOC content, (b) decay-corrected F<sup>14</sup>C and δ<sup>13</sup>C for bulk OC with their potential sources, including petrogenic OC, terrestrial biospheric OC and marine OC (see text for reference), and cross plot of (c) δ<sup>13</sup>C and (d) decay-corrected F<sup>14</sup>C of bulk OC and C<sub>28+30</sub> FAs as a function of TOC or mean grain size in two cores, respectively.

after ~1974. Yet, the convergence of the C<sub>28+30</sub> FAs and bulk POC isotope signals in both cores also indicates homogenization of terrestrial POC occurred annually during the winter transport (Ge et al., 2014).

To conclude, the terrestrial biospheric OC composition changed through time as shown by variations of δ<sup>13</sup>C<sub>C<sub>28+30</sub>FAs</sub> and F<sup>14</sup>C<sub>C<sub>28+30</sub>FAs</sub> values, implying two periods of elevated fresh C<sub>4</sub> plant export from the PR at the proximal site in the 1950s and after ~1974, respectively.

#### 4.2.3. Fractional Contributions of POC Components From Different Sources

Using a Bayesian Markov chain model, we calculated the fractional POC contributions from terrestrial biospheric, petrogenic and marine sources to infer their respective burial fluxes, with exception of the contribution from riverine primary production as this POC pool is readily degraded prior to burial in the coastal sediments (Wei et al., 2020). For the purpose of this study, we focus on terrestrial POC burial, but marine POC contributions

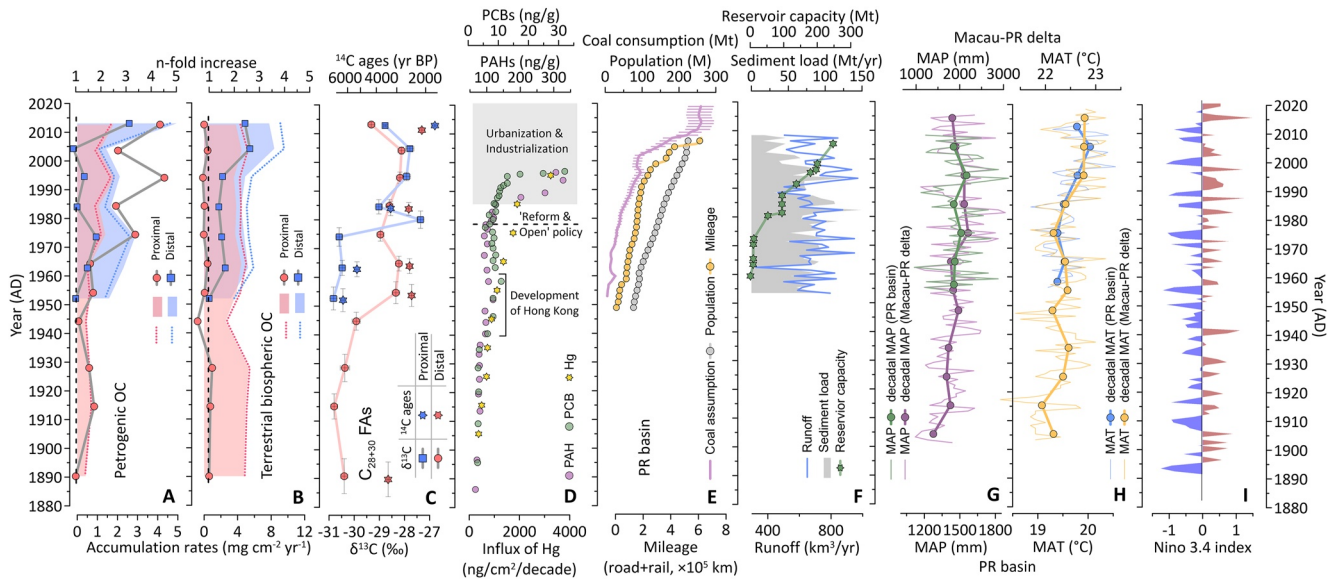


**Figure 5.** Variations of (a) accumulation rates of petrogenic OC (filled areas) and the corresponding n-fold increase (symbols), as well as (b) accumulation rates of terrestrial biospheric OC (filled areas) and the corresponding n-fold increase (symbols). In Panel A and B, the dashed lines represent accumulation rates of petrogenic and terrestrial biospheric OC, respectively, based on a simplified Monte Carlo simulation. Variations of (c)  $\delta^{13}\text{C}$  (squares) and  $^{14}\text{C}$  ages (stars) of  $\text{C}_{28+30}$  FAs in the proximal (light red) and distal cores (light blue), (d) pollutant concentration (polycyclic aromatic hydrocarbons, PAHs, light grape circles, Liu, Colin, et al., 2005; polychlorinated biphenyls, PCBs, light green circles, Mai et al., 2005) and influx of heavy metal (Hg, light yellow stars, Qi et al., 2010) in sediment cores from the Pearl River estuary, (e) population (gray circles, DCSNBS, 2010), coal consumption (light grape curve with error bar; the uncertainty of coal assumption is calculated using a standard deviation value for the relative proportion contributed to the Pearl River basin between 1990 and 2019; NBSC, 2019), as well as mileage of road and railway in the Pearl River basin (light yellow circles, DCSNBS, 2010), (f) river runoff (light blue curve), sediment load (gray areas) and reservoir storage capacity (light yellow circles, Wu et al., 2012). The PR sediment load in panel f is integrated based on data from eight hydrological stations (six in the West River and two in the East and North Rivers) upstream of the Pearl River Delta (Wu et al., 2012). (g) and (h) Instrumental mean annual precipitation (MAP, thin curve) and mean decadal precipitation (thick curve with circles) in the Pearl River basin and delta (Macau), respectively (MMGB, 2023; Tian, 2016). (i) Oceanic Niño Index (Nino 3.4 region, filled area, [https://psl.noaa.gov/gcos\\_wgsp/Timeseries/Nino34/](https://psl.noaa.gov/gcos_wgsp/Timeseries/Nino34/), Rayner et al., 2003).

show an overall increasing trend at both sites through time, consistent with previous observations documenting the effects of eutrophication (Supplementary Table S5 in Supporting Information S1; Hu et al., 2008; Jia et al., 2013). The accumulation rates of terrestrial biospheric POC ( $\text{AR}_{\text{TB}}$ ) and petrogenic OC ( $\text{AR}_{\text{p}}$ ) are calculated by multiplying proportions of each POC with POC accumulation rate (Figures 5a and 5b). Bayesian Markov chain model results were obtained using both coal fly ash-derived POC or bedrock-derived OC as the endmember value for petrogenic OC. Both models reveal similar AR trends through time, with an average relative difference of  $9 \pm 7\%$  for  $\text{AR}_{\text{TB}}$  and  $9 \pm 4\%$  for  $\text{AR}_{\text{p}}$  (Table S5 in Supporting Information S1). These small differences suggest our endmember apportionments are comparable irrespective of potential compositional changes in the petrogenic POC endmember through time, that is,  $\text{AR}_{\text{p}}$  estimates are largely independent from changes in the relative contributions from bedrock and coal fly ash to the total petrogenic POC pool (which we cannot calculate given the similarity of the isotope endmember values of these sources). Post-1970s, the  $\text{AR}_{\text{p}}$  value was on average 2.4-times higher than pre-1970s at the proximal site, indicating increased petrogenic POC export from the PR. The  $\text{AR}_{\text{p}}$  values at the distal site were comparable to those at the proximal site after the 1970s, but higher values were also evident in those depths characterized by relict sediment input as well as at the core-top (Figure 5b). In contrast,  $\text{AR}_{\text{TB}}$  showed relatively minor changes at the proximal site, but increased at the distal site, particularly after 2000 (Figure 5a). Another Monte Carlo simulation approach (based on the core algorithm of an inverse matrix; Andersson, 2011) was previously used in similar studies in the China marginal seas (e.g., Tao et al., 2016; Wei et al., 2021a; P. Yao et al., 2015; Yu et al., 2021) and was also applied in this study. Both models show similar AR variations over time with an average relative difference of  $12 \pm 5\%$  for  $\text{AR}_{\text{TB}}$  and  $13 \pm 6\%$  for  $\text{AR}_{\text{p}}$  (Figures 5a and 5b), confirming the robustness of our Bayesian Markov chain model for further interpretation.

### 4.3. Controls on Changes in Terrestrial OC Composition

Both climatic changes and human perturbations (e.g., land use changes and river management) in the river watershed probably affect the quantity and quality of the exported riverine terrestrial POC (Eglinton et al., 2021; Kusch et al., 2021a, 2021b; Regnier et al., 2013).  $C_3$  plants dominate the natural vegetation in the PR watershed (Figure 1c) with only minor presence of  $C_4$  grasses in upland areas (Yu et al., 2010). However, enhanced  $C_4$  plant coverage following the modification of agricultural practices, urbanization and deforestation, particularly in lowland areas, seems to have resulted in increased  $C_4$  plant export to the coastal ocean as implied by the increasing  $\delta^{13}C_{28+30FAs}$  and  $F^{14}C_{28+30FAs}$  values through time. Increasing  $F^{14}C_{28+30FAs}$  values are unlikely a function of more enriched bomb- $^{14}C$  signal or increased bomb- $^{14}C$  incorporation because of the concurrent changes in  $\delta^{13}C_{28+30FAs}$  and  $F^{14}C_{28+30FAs}$  values. We interpret these effects mainly based on the proximal core data due to its proximity to the PR delta and therefore more direct record of changes in the PR lowland ecosystem. The mean annual temperature (MAT) and precipitation (MAP) in the PR basin show similar variations to those recorded in Macau (i.e., the PR delta), and are characterized by decadal ENSO fluctuations (Figures 5g–5i). After smoothing the MAT and MAP of the PR delta by 10-yr averaging, we observe a 0.8°C increase of MAT over the last century as well as an increase of MAP of about 80 cm during the 1900s–1970s followed by a decrease of roughly 40 cm in the 2010s (Figures 5g and 5h). Increased MAT and MAP should lead to lower  $\delta^{13}C$  values of  $C_3/C_4$  plants or surface soil POC (Rao et al., 2017), but we observe the opposite relationship in the two cores. Moreover, a recent global investigation suggests that  $^{14}C$  ages of river-exported long-chain FAs have significant negative relationship with MAT and MAP:  $\log_{10} (^{14}C \text{ age})$  versus MAT, slope =  $-0.036 \pm 0.004$ ;  $\log_{10} (^{14}C \text{ age})$  versus  $\log_{10} (\text{MAP})$ , (slope =  $-1.46$ ; Eglinton et al., 2021). Using these regressions, we estimate the magnitude of changes in  $^{14}C$  ages of long-chain FAs that could be directly linked to the changes in MAT and MAP. If the MAT and MAP variations affected PR-exported  $^{14}C_{28+30FAs}$  ages, we could expect a 30-yr decrease of  $^{14}C_{28+30FAs}$  ages caused by MAT increase over the last century as well as a 300-yr decrease (1900s–1970s) and a 100-yr increase (after the 1970s) controlled by MAP. These shifts are significantly smaller than the observed  $^{14}C_{28+30FAs}$  changes in both cores (Figure 3c). Therefore, these small changes in MAT and MAP in the PR basin and delta are unlikely responsible for substantial ecosystem/vegetation shifts. Instead, the observed shifts toward increased  $AR_p$ ,  $AR_{TB}$  and  $\delta^{13}C_{28+30FAs}$ , as well as decreased  $C_{28+30FAs}$  ages, agree well with intensified human perturbation of the PR system since the 1950s, as evidenced by accelerated population growth, land use changes and river management (Figures 5e and 5f).

We link the first compositional change of buried terrestrial biospheric POC around the 1950s to extensive wartime deforestation and modifications in agricultural practices post-World War II, which were characterized by the introduction of  $C_4$  grasses and crops (e.g., sugar cane and corn) in the PR lowland areas (Owen & Lee, 2004). The second compositional change of terrestrial biospheric POC since the mid-1970s agrees in timing with increased urbanization and industrialization in the PR delta augmented by the establishment of China's “Reform and Open” policy in 1978. Even if terrestrial OC is exported quickly, lowland ecosystem changes could be recorded in estuarine and coastal sediments with a potential 5–10 yr delay (estimated from the pronounced increases in anthropogenic pollutants and heavy metal contamination relative to the establishment of the “Reform and Open” policy as suggested in previous studies, Figure 5d), which is longer than the age model uncertainties for the proximal (<2.8 yr) and distal cores (<2.4 yr) in the 1970s. Thus, the second change could possibly also be controlled or augmented by other factors, such as river management since the 1960s. Damming in the PR upland areas (Figures 1a and 5f) likely reduced runoff and sediment loads from the upland areas and resulted in preferential transport of finer mineral particles to the ocean as observed by the decrease of mean grain size in our coastal sediment cores irrespective of seabed reworking effects (Figure 3a). As a result, an increased proportion of lowland-derived terrestrial biospheric POC was buried in the coastal ocean. Although agricultural practices, urbanization and deforestation in PR lowland areas may have accelerated erosion of terrestrial biospheric POC, subsequent deep-soil erosion and associated export of older terrestrial biospheric POC could have been impeded by the concurrent river embankment (Shen et al., 2021). Embankment increased since the 1960s, particularly in the PR delta where the PR diverges into a network of many small rivers intertwined with numerous croplands and urban built-up areas. The effects of embankment in the PR delta gradually increased and, as mentioned above, as of 2013 a total length of 28,900 km in this area has been embanked. However, we acknowledge that we cannot assess this effect in detail based on the lack of records reporting embankment through time. Thus, we attribute the insignificant  $AR_{TB}$  variation (especially at the proximal site) to a reduction of the mean soil erosion depth (toward top-soil erosion only) in deforested, urban and agricultural areas with expanded  $C_4$  grasses and croplands in the PR delta, which collectively account for 37% of the PR delta area today (Figure 1c).

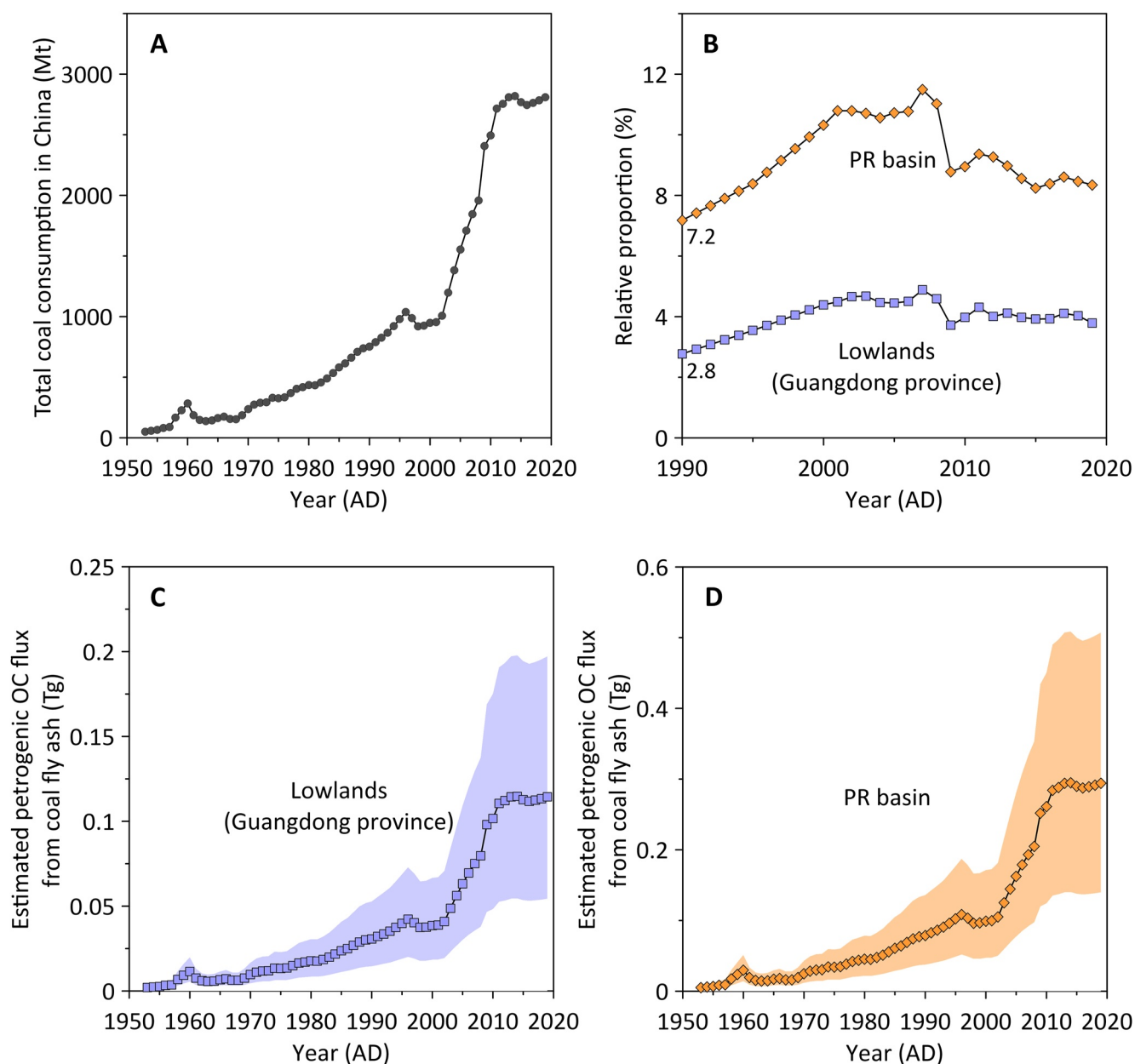


**Figure 6.** Time series of (a) annual coal consumption in China from 1953 to 2019 (DCSNBS, 2010; NBSC, 2019), (b) relative proportion of coal consumption in the lowlands and the entire PR basin from 1990 to 2019, as well as the estimated petrogenic OC flux from coal fly ash in (c) the lowlands and (d) the entire PR basin between 1953 and 2019 (color bars represent uncertainties of estimation).

Elevated  $AR_p$  at the proximal site since the 1970s suggest increasing petrogenic POC export from the PR basin. Since deep-soil erosion in the PR delta apparently weakened, we expect that potential petrogenic POC contributions from this source should have decreased as well. In contrast, petrogenic POC from riverbed erosion could have been enhanced in the mid-lower reaches of the river. This is because damming reduces sediment loads from upland areas, changing the mid-lower reaches from sinks to sources of river sediments and POC, when the sediment carrying capacity of the river flow exceeds the suspend sediment concentration (Yang et al., 2019). However, the significance of petrogenic POC from this source remains to be determined as biospheric rather than petrogenic POC dominates POC in riverbed sediments (Lin et al., 2019). On the other hand, coal fly ash input may have increased in parallel with the increased coal consumption in China since the 1950s (Figure 6a) and the data from G. Q. Liu et al. (2005) show that PAHs (Figure 5d) mostly have a pyrolytic origin consistent with coal

burning. Thus, we calculated the flux of petrogenic POC from coal fly ash according to the following equation (Li et al., 2021):

$$F_{ash-OC} = F_{coal} \times f_{ash} \times f_{non-utilized-ash} \times [OC]_{ash} \quad (6)$$

where  $F_{coal}$  is coal consumption,  $f_{ash}$  is the fly ash content,  $f_{non-utilized-ash}$  is the fraction of non-utilized fly ash, and  $[OC]_{ash}$  is the petrogenic POC content in the fly ash. Coal consumption data for the lowlands (i.e., Guangdong province) and the entire PR basin are only available from 1990 to 2019, showing that these areas account for 2.8%–4.9% and 7.2%–11.5% of national coal consumption, respectively (Figure 6b). The utilized rate of coal-fly ash in China was below 62% prior to 2001 and increased to 70% between 2001 and 2015 (Li et al., 2021). Based on the average fly ash content of 17% in coal and an average petrogenic OC content of 2.25% in coal fly ash from northern China (Li et al., 2021), as well as the average proportions of 2.8% and 7.2% in the domestic consumption for either the lowlands or the entire PR basin, we estimate petrogenic POC fluxes from coal fly ash increased from 0.002 to 0.114 Tg C yr<sup>-1</sup> for the PR lowlands and from 0.005 to 0.294 Tg C yr<sup>-1</sup> for entire PR basin during 1950–2020, respectively (Figures 6c and 6d). We acknowledge such a simplified estimation requires further constraints in the future by, for example, extending coal consumption data coverage (pre-1990) and refining fly ash-derived petrogenic POC data. Nonetheless, this estimated flux is on a similar order of magnitude as the burial flux ( $0.1 \pm 0.01$  Tg C yr<sup>-1</sup>) of petrogenic POC in surface sediments of the PR-derived coastal mudbelt (Wei et al., 2021a). Wei et al. (2021a) showed that the PR-derived petrogenic POC in the coastal ocean is highly refractory and experiences little oxidation during further dispersal along the mudbelt, although growing evidence elsewhere suggests that petrogenic POC can be partly oxidized during transport in different settings (Blattmann, 2022; Blattmann et al., 2018a, 2018b; Horan et al., 2017, 2019). This discordance can be reconciled by assuming that coal fly ash is a major source of petrogenic POC in the two cores investigated here, because petrogenic OC from coal fly ash is highly recalcitrant and unreactive whereas the bedrock-derived petrogenic POC present elsewhere is relatively more labile and more easily oxidized (e.g., Bird et al., 2015; Li et al., 2021). Thus, the elevated AR<sub>p</sub> likely reflects increased production and subsequent export of coal fly ash to the ocean driven by increasing coal consumption in the PR basin associated with industrialization.

Overall, our observations in the coastal sediment cores suggest a two-step history of anthropogenic perturbation of the PR ecosystem and associated POC export: (a) agricultural practices and deforestation during the 1930s–1950s leading to an ecosystem change toward more C<sub>4</sub> plants but a relatively small effect on export fluxes of terrestrial OC sub-pools; and (b) increasing export of petrogenic POC likely from fly ash and increasing export of relatively fresh terrestrial biospheric POC to the coastal ocean presumably caused by increasing coal consumption and river management, respectively, in the lowland areas.

## 5. Implications and Conclusions

Global terrestrial POC export to the ocean is increasingly affected by anthropogenic perturbation, including land use changes (i.e., agriculture and urbanization), river management (i.e., damming and embankment) and fossil fuel combustion (Regnier et al., 2013). According to process-based arguments and models, these human activities have led to the export of an additional ~100 Tg C yr<sup>-1</sup> of anthropogenically altered C to the ocean, which at present is mainly buried in coastal sediments (Regnier et al., 2022). However, this estimation quantifies only total terrestrial carbon fluxes without assessing the changes in the flux of POC sub-pools and lacks observational evidence, which impedes a thorough understanding of the anthropogenic influence on the global carbon cycle. In the PR watershed, coal consumption in the lowland areas has likely led to increasing petrogenic POC export to the coastal depocenters, presumably predominantly from coal fly ash whereas the export of bedrock derived POC from upland areas has likely decreased. Such an origin is consistent with published PAH data (G. Q. Liu et al., 2005), and the highly recalcitrant and unreactive nature of coal fly ash (Li et al., 2021) can explain the increased burial flux of petrogenic OC to the coastal ocean since the 1970s. However, we acknowledge that additional data are required to independently confirm a coal fly ash origin. In contrast, about 50% of terrestrial biospheric POC is lost by remineralization before final burial in the region, supposedly caused by repeated suspension-deposition loops, cumulative oxygen exposure, and repetitive redox oscillations during transport (Wei et al., 2021a). Considering elevated coastal OC production due to increased anthropogenic eutrophication since the Industrial Age (Regnier et al., 2013), remineralization of terrestrial biospheric POC may be further facilitated by the supply of reactive marine POC enhancing microbial breakdown, that is, priming effects. Nonetheless,

we still observe an overall increased burial of fresh terrestrial biospheric POC from an intensively perturbed or altered terrestrial ecosystems, which, if protected from subsequent microbial degradation, contributes to the long-term, geological carbon sink (Hilton & West, 2020).

Many large fluvial systems in densely populated regions have been undergoing similar anthropogenic perturbations as observed for the PR basin (Grill et al., 2019). For example, increasing coal combustion in the Yangtze River basin seems to have increased export of fly ash-derived petrogenic POC to the coastal ocean and increasing dam construction has led to decreased bedrock-derived petrogenic POC export from upland areas. In contrast, embankment in the lower Mississippi River has reduced the sediment exchange between river and floodplain by 90%, which effectively prevents erosion of older POC from the floodplain and expedites export of younger POC to the coastal ocean (Shen et al., 2021). Above observations and our data from the PR ecosystem demonstrate the complex and contrasting effects diverse anthropogenic perturbation processes impart on the burial fluxes of terrestrial POC sub-pools. Our approach allows for the deconvolution of qualitative and quantitative changes in burial fluxes, which are hidden at the bulk level, and thus aids a more thorough understanding of carbon cycle feedback mechanisms to anthropogenic forcing and the proper assessment of sources and sinks of anthropogenic CO<sub>2</sub> in the Industrial Age.

### Data Availability Statement

Data generated for this study are uploaded as supplementary material and published in the PANGAEA data repository (Wei et al., 2021b).

### Acknowledgments

This work is supported by the China Post-doctoral Science Foundation (No. 2021M692410), the National Natural Science Foundation of China (No. 41676030 and 42030504), and the China Scholarship Council (No. 201706260033), as well as the institutional funding of the AWI. We appreciate Dr. Feng Ye for providing samples, Dr. Yijing Wu for <sup>210</sup>Pb measurement, Ralph Kreuz at MARUM for stable carbon isotope analysis, and all members of the Marine Geochemistry Laboratory at AWI for AMS measurements.

### References

- Andersson, A. (2011). A systematic examination of a random sampling strategy for source apportionment calculations. *Science of the Total Environment*, 412–413, 232–238. <https://doi.org/10.1016/j.scitotenv.2011.10.031>
- Bao, R., McIntyre, C., Zhao, M., Zhu, C., Kao, S. J., & Eglinton, T. I. (2016). Widespread dispersal and aging of organic carbon in shallow marginal seas. *Geology*, 44(10), 791–794. <https://doi.org/10.1130/G37948.1>
- Bauer, J. E., Cai, W. J., Raymond, P. A., Bianchi, T. S., Hopkinson, C. S., & Regnier, P. A. G. (2013). The changing carbon cycle of the coastal ocean. *Nature*, 504(7478), 61–70. <https://doi.org/10.1038/nature12857>
- Bird, M. I., Wynn, J. G., Saiz, G., Wurster, C. M., & McBeath, A. (2015). The pyrogenic carbon cycle. *Annual Review of Earth and Planetary Sciences*, 43(1), 273–298. <https://doi.org/10.1146/annurev-earth-060614-105038>
- Blair, N. E., & Aller, R. C. (2012). The fate of terrestrial organic carbon in the Marine environment. *Annual Review of Marine Science*, 4(1), 401–423. <https://doi.org/10.1146/annurev-marine-120709-142717>
- Blattmann, T. M. (2022). Ideas and perspectives: Emerging contours of a dynamic exogenous kerogen cycle. *Biogeosciences*, 19(2), 359–373. <https://doi.org/10.5194/bg-19-359-2022>
- Blattmann, T. M., Letsch, D., & Eglinton, T. I. (2018a). On the geological and scientific legacy of petrogenic organic carbon. *American Journal of Science*, 318(8), 861–881. <https://doi.org/10.2475/08.2018.02>
- Blattmann, T. M., Zhang, Y., Zhao, Y., Wen, K., Lin, S., Li, J., et al. (2018b). Contrasting fates of petrogenic and biospheric carbon in the South China Sea. *Geophysical Research Letters*, 45(17), 9077–9086. <https://doi.org/10.1029/2018GL079222>
- Bosch, C., Andersson, A., Krusá, M., Bandh, C., Hovorková, I., Klánová, J., et al. (2015). Source apportionment of polycyclic Aromatic hydrocarbons in central European soils with compound-specific triple isotopes ( $\delta^{13}\text{C}$ ,  $\Delta^{14}\text{C}$ , and  $\delta^2\text{H}$ ). *Environmental Science and Technology*, 49(13), 7657–7665. <https://doi.org/10.1021/acs.est.5b01190>
- Cai, F., Su, X., Liu, J., Li, B., & Lei, G. (2009). Coastal erosion in China under the condition of global climate change and measures for its prevention. *Progress in Natural Science*, 19(4), 415–426. <https://doi.org/10.1016/j.pnsc.2008.05.034>
- Cerling, T. E., Harris, J. M., MacFadden, B. J., Leakey, M. G., Quade, J., Eisenmann, V., & Ehleringer, J. R. (1997). Global vegetation change through the Miocene/Pliocene boundary. *Nature*, 389(6647), 153–158. <https://doi.org/10.1038/38229>
- Chen, F., Zhang, L., Yang, Y., & Zhang, D. (2008). Chemical and isotopic alteration of organic matter during early diagenesis: Evidence from the coastal area off-shore the Pearl River estuary, south China. *Journal of Marine Systems*, 74(1–2), 372–380. <https://doi.org/10.1016/j.jmarsys.2008.02.004>
- Chen, J., Ban, Y., & Li, S. (2014). China: Open access to Earth land-cover map. *Nature*, 514(7523), 434. <https://doi.org/10.1038/514434c>
- Cui, Y., Bercovici, A., Yu, J., Kump, L. R., Freeman, K. H., Su, S., & Vajda, V. (2017). Carbon cycle perturbation expressed in terrestrial Permian–Triassic boundary sections in South China. *Global and Planetary Change*, 148, 272–285. <https://doi.org/10.1016/j.gloplacha.2015.10.018>
- Dai, S. B., Yang, S. L., & Cai, A. M. (2008). Impacts of dams on the sediment flux of the Pearl River, southern China. *Catena*, 76(1), 36–43. <https://doi.org/10.1016/j.catena.2008.08.004>
- Department of Comprehensive Statistics of National Bureau of Statistics (DCSNBS). (2010). China compendium of statistics 1949–2008 [Dataset]. China Statistics Press. Retrieved from [http://www.stats.gov.cn/english/NewsEvents/200601/t20060113\\_25725.html](http://www.stats.gov.cn/english/NewsEvents/200601/t20060113_25725.html)
- Ding, L., Qi, Y., Shan, S., Ge, T., Luo, C., & Wang, X. (2020). Radiocarbon in dissolved organic and inorganic carbon of the South China Sea. *Journal of Geophysical Research: Oceans*, 125(4), 1–14. <https://doi.org/10.1029/2020jc016073>
- Dong, L., Su, J., Li, Y., Xia, X., & Guan, W. (2006). Physical processes and sediment dynamic in the Pearl River. In E. Wolanski (Ed.), *The environment in Asia Pacific harbours*. Springer. <https://doi.org/10.1007/1-4020-3655-8>
- Druffel, E. R. M., & Benavides, L. M. (1986). Input of excess CO<sub>2</sub> to the surface ocean based on <sup>13</sup>C/<sup>12</sup>C ratios in a banded Jamaican sclerosponge. *Nature*, 321(6065), 58–61. <https://doi.org/10.1038/321058a0>
- Eglinton, T., Galy, V., Hemingway, J., Feng, X., Bao, H., Blattmann, T. M., et al. (2021). Climate control on terrestrial biospheric carbon turnover. *Proceedings of the National Academy of Sciences of the United States of America*, 118(8). <https://doi.org/10.1073/pnas.2011585118>

- Fahrni, S. M., Wacker, L., Synal, H. A., & Szidat, S. (2013). Improving a gas ion source for 14C AMS. *Nuclear Instruments and Methods in Physics Research, Section B: Beam Interactions with Materials and Atoms*, 294, 320–327. <https://doi.org/10.1016/j.nimb.2012.03.037>
- French, K. L., Hein, C. J., Haghypour, N., Wacker, L., Kudrass, H. R., Eglinton, T. I., & Galy, V. (2018). Millennial soil retention of terrestrial organic matter deposited in the Bengal Fan. *Scientific Reports*, 8(1), 1–8. <https://doi.org/10.1038/s41598-018-30091-8>
- Galy, V., & Eglinton, T. (2011). Protracted storage of biospheric carbon in the Ganges–Brahmaputra basin. *Nature Geoscience*, 4(12), 843–847. <https://doi.org/10.1038/ngeo1293>
- Galy, V., Eglinton, T., France-Lanord, C., & Sylva, S. (2011). The provenance of vegetation and environmental signatures encoded in vascular plant biomarkers carried by the Ganges-Brahmaputra rivers. *Earth and Planetary Science Letters*, 304(1–2), 1–12. <https://doi.org/10.1016/j.epsl.2011.02.003>
- Galy, V., France-Lanord, C., Beyssac, O., Faure, P., Kudrass, H., & Palhol, F. (2007). Efficient organic carbon burial in the Bengal fan sustained by the Himalayan erosional system. *Nature*, 450(7168), 407–410. <https://doi.org/10.1038/nature06273>
- Galy, V., Peucker-Ehrenbrink, B., & Eglinton, T. (2015). Global carbon export from the terrestrial biosphere controlled by erosion. *Nature*, 521(7551), 204–207. <https://doi.org/10.1038/nature14400>
- Gao, P., Zhou, L., Liu, K., & Xu, X. (2019). Radiocarbon in the maritime air and sea surface water of the South China Sea. *Radiocarbon*, 61(2), 461–472. <https://doi.org/10.1017/RDC.2018.100>
- Gao, S., Liu, Y., Yang, Y., Liu, P. J., Zhang, Y., & Wang, Y. P. (2015). Evolution status of the distal mud deposit associated with the Pearl River, northern South China Sea continental shelf. *Journal of Asian Earth Sciences*, 114, 562–573. <https://doi.org/10.1016/j.jseas.2015.07.024>
- Ge, Q., Liu, J. P., Xue, Z., & Chu, F. (2014). Dispersal of the Zhujiang River (Pearl River) derived sediment in the Holocene. *Acta Oceanologica Sinica*, 33(8), 1–9. <https://doi.org/10.1007/s13131-014-0407-8>
- Goñi, M. A. (1997). Record of terrestrial organic matter composition in Amazon Fan sediments. In *Proceedings of the ocean drilling program, 155 scientific results, (May)*. <https://doi.org/10.2973/odp.proc.sr.155.240.1997>
- Goñi, M. A., Ruttnerberg, K. C., & Eglinton, T. I. (1997). Sources and contribution of terrigenous organic carbon to surface sediments in the Gulf of Mexico. *Nature*, 389(6648), 275–278. <https://doi.org/10.1038/38477>
- Graven, H., Allison, C. E., Etheridge, D. M., Hammer, S., Keeling, R. F., Levin, I., et al. (2017). Compiled records of carbon isotopes in atmospheric CO<sub>2</sub> for historical simulations in CMIP6. *Geoscientific Model Development*, 10(12), 4405–4417. <https://doi.org/10.5194/gmd-10-4405-2017>
- Grill, G., Lehner, B., Thieme, M., Geenen, B., Tickner, D., Antonelli, F., et al. (2019). Mapping the world's free-flowing rivers. *Nature*, 569(7755), 215–221. <https://doi.org/10.1038/s41586-019-1111-9>
- He, B., Dai, M., Huang, W., Liu, Q., Chen, H., & Xu, L. (2010). Sources and accumulation of organic carbon in the Pearl River Estuary surface sediment as indicated by elemental, stable carbon isotopic, and carbohydrate compositions. *Biogeosciences*, 7(10), 3343–3362. <https://doi.org/10.5194/bg-7-3343-2010>
- Hemingway, J. D., Schefuß, E., Dinga, B. J., Pryer, H., & Galy, V. V. (2016). Multiple plant-wax compounds record differential sources and ecosystem structure in large river catchments. *Geochimica et Cosmochimica Acta*, 184, 20–40. <https://doi.org/10.1016/j.gca.2016.04.003>
- Hilton, R. G., & West, A. J. (2020). Mountains, erosion and the carbon cycle. *Nature Reviews Earth & Environment*, 1(June), 284–299. <https://doi.org/10.1038/s43017-020-0058-6>
- Horan, K., Hilton, R. G., Dellinger, M., Tipper, E., Galy, V., Calmels, D., et al. (2019). Carbon dioxide emissions by rock organic carbon oxidation and the net geochemical carbon budget of the Mackenzie River Basin. *American Journal of Science*, 319(6), 473–499. <https://doi.org/10.2475/06.2019.02>
- Horan, K., Hilton, R. G., Selby, D., Ottley, C. J., Gröcke, D. R., Hicks, M., & Burton, K. W. (2017). Mountain glaciation drives rapid oxidation of rock-bound organic carbon (pp. 1–9).
- Hu, J., Zhang, G., Li, K., Peng, P., & Chivas, A. R. (2008). Increased eutrophication offshore Hong Kong, China during the past 75 years: Evidence from high-resolution sedimentary records. *Marine Chemistry*, 110(1–2), 7–17. <https://doi.org/10.1016/j.marchem.2008.02.001>
- Jia, G., Xu, S., Chen, W., Lei, F., Bai, Y., & Huh, C. A. (2013). 100-year ecosystem history elucidated from inner shelf sediments off the Pearl River estuary, China. *Marine Chemistry*, 151, 47–55. <https://doi.org/10.1016/j.marchem.2013.02.005>
- Kusch, S., Mollenhauer, G., Willmes, C., Hefter, J., Eglinton, T. I., & Galy, V. (2021). Controls on the age of plant waxes in marine sediments – A global synthesis. *Organic Geochemistry*, 157, 104259. <https://doi.org/10.1016/j.orgchem.2021.104259>
- Kusch, S., Rethemeyer, J., Ransby, D., & Mollenhauer, G. (2021). Permafrost organic carbon turnover and export into a high-Arctic fjord: A case study from Svalbard using compound-specific 14C analysis. *Journal of Geophysical Research: Biogeosciences*, 126(3), e2020JG006008. <https://doi.org/10.1029/2020jg006008>
- Kusch, S., Rethemeyer, J., Schefuß, E., & Mollenhauer, G. (2010). Controls on the age of vascular plant biomarkers in Black Sea sediments. *Geochimica et Cosmochimica Acta*, 74(24), 7031–7047. <https://doi.org/10.1016/j.gca.2010.09.005>
- Li, G. K., Fischer, W. W., Lamb, M. P., West, A. J., Zhang, T., Galy, V., et al. (2021). Coal fly ash is a major carbon flux in the Chang Jiang (Yangtze River) basin. *Proceedings of the National Academy of Sciences of the United States of America*, 118(21), e1921544118. <https://doi.org/10.1073/pnas.1921544118>
- Li, T., & Li, T. J. (2017). Sediment transport processes in the Pearl River Estuary as revealed by grain-size end-member modeling and sediment trend analysis. *Geo-Marine Letters*, 38(2), 1–12. <https://doi.org/10.1007/s00367-017-0518-2>
- Li, X., Zhang, Z., Wade, T. L., Knap, A. H., & Zhang, C. L. (2017). Sources and compositional distribution of organic carbon in surface sediments from the lower Pearl River to the coastal South China Sea. *Journal of Geophysical Research: Biogeosciences*, 122(8), 2104–2117. <https://doi.org/10.1002/2017JG003981>
- Lin, B., Liu, Z., Eglinton, T. I., Kandasamy, S., Blattmann, T. M., Haghypour, N., & de Lange, G. J. (2019). Perspectives on provenance and alteration of suspended and sedimentary organic matter in the subtropical Pearl River system, South China. *Geochimica et Cosmochimica Acta*, 259, 270–287. <https://doi.org/10.1016/j.gca.2019.06.018>
- Liu, G. Q., Zhang, G., Li, X. D., Li, J., Peng, X. Z., & Qi, S. H. (2005). Sedimentary record of polycyclic aromatic hydrocarbons in a sediment core from the Pearl River Estuary, South China. *Marine Pollution Bulletin*, 51(8–12), 912–921. <https://doi.org/10.1016/j.marpolbul.2005.02.038>
- Liu, Y., Liu, G., Yousaf, B., Zhang, J., & Zhou, L. (2020). Carbon fractionation and stable carbon isotopic fingerprint of road dusts near coal power plant with emphases on coal-related source apportionment. *Ecotoxicology and Environmental Safety*, 202, 110888. <https://doi.org/10.1016/j.ecoenv.2020.110888>
- Liu, Z., Colin, C., Trentesaux, A., Siani, G., Frank, N., Blamart, D., & Farid, S. (2005). Late Quaternary climatic control on erosion and weathering in the eastern Tibetan Plateau and the Mekong Basin. *Quaternary Research*, 63(3), 316–328. <https://doi.org/10.1016/j.yqres.2005.02.005>
- Macao Meteorological and Geophysical Bureau (MMGB). (2023). Macao meteorological and geophysical bureau [Dataset]. FRAME. Retrieved from <https://frame.smg.gov.mo/centenary/index.htm>

- Mai, B., Zeng, E. Y., Luo, X., Yang, Q., Zhang, G., Li, X., et al. (2005). Abundances, depositional fluxes, and homologue patterns of polychlorinated biphenyls in dated sediment cores from the Pearl River Delta, China. *Environmental Science and Technology*, 39(1), 49–56. <https://doi.org/10.1021/es049015d>
- McLaren, P. (1985). The effects of sediment transport on grain-size distributions. *Journal of Sedimentary Research*, 55(4). <https://doi.org/10.1306/212F86FC-2B24-11D7-8648000102C1865D>
- Mei, W., & Xie, S. P. (2016). Intensification of landfalling typhoons over the northwest Pacific since the late 1970s. *Nature Geoscience*, 9(10), 753–757. <https://doi.org/10.1038/ngeo2792>
- Ministry of water resources and national bureau of Statistics (MWR&NBS). (2013). Bulletin of first national census for water: Guangdong. *Information for Decision Magazine*, 14. CNKI:SUN:LJDC.2013-14-028.
- Mitsuguchi, T., Dang, P. X., Kitagawa, H., Yoneda, M., & Shibata, Y. (2007). Tropical South China Sea surface <sup>14</sup>C record in an annually-banded coral. *Radiocarbon*, 49(2), 905–914. <https://doi.org/10.1017/S003822200042776>
- Mollenhauer, G., & Eglinton, T. I. (2007). Diagenetic and sedimentological controls on the composition of organic matter preserved in California Borderland Basin sediments. *Limnology & Oceanography*, 52(2), 558–576. <https://doi.org/10.4319/lo.2007.52.2.0558>
- Mollenhauer, G., Grotheer, H., Gentz, T., Bonk, E., & Hefter, J. (2021). Standard operation procedures and performance of the MICADAS radiocarbon laboratory at Alfred Wegener Institute (AWI), Germany. *Nuclear Instruments and Methods in Physics Research Section B: Beam Interactions with Materials and Atoms*, 496, 45–51. <https://doi.org/10.1016/j.nimb.2021.03.016>
- National Bureau of Statistics of China (NBSC). (2019). China statistical year book [Dataset]. China Statistics Press. Retrieved from <http://www.stats.gov.cn/sj/ndsj/2019/indexch.htm>
- Owen, R. B., & Lee, R. (2004). Human impacts on organic matter sedimentation in a proximal shelf setting, Hong Kong. *Continental Shelf Research*, 24(4–5), 583–602. <https://doi.org/10.1016/j.csr.2003.11.004>
- Qi, S., Leipe, T., Rueckert, P., Di, Z., & Harff, J. (2010). Geochemical sources, deposition and enrichment of heavy metals in short sediment cores from the Pearl River Estuary, Southern China. *Journal of Marine Systems*, 82, S28–S42. <https://doi.org/10.1016/j.jmarsys.2010.02.003>
- Rao, Z., Guo, W., Cao, J., Shi, F., Jiang, H., & Li, C. (2017). Relationship between the stable carbon isotopic composition of modern plants and surface soils and climate: A global review. *Earth-Science Reviews*, 165, 110–119. <https://doi.org/10.1016/j.earscirev.2016.12.007>
- Rayner, N. A., Parker, D. E., Horton, E. B., Folland, C. K., Alexander, L. V., Rowell, D. P., et al. (2003). Global analyses of sea surface temperature, sea ice, and night marine air temperature since the late nineteenth century. *Journal of Geophysical Research*, 108(D14), 4407. <https://doi.org/10.1029/2002JD002670>
- Regnier, P., Friedlingstein, P., Ciais, P., Mackenzie, F. T., Gruber, N., Janssens, I. A., et al. (2013). Anthropogenic perturbation of the carbon fluxes from land to ocean. *Nature Geoscience*, 6(8), 597–607. <https://doi.org/10.1038/ngeo1830>
- Regnier, P., Resplandy, L., Najjar, R. G., & Ciais, P. (2022). The land-to-ocean loops of the global carbon cycle. *Nature*, 603(7901), 401–410. <https://doi.org/10.1038/s41586-021-04339-9>
- Reimer, P. J., Brown, T. A., & Reimer, R. W. (2004). Discussion: Reporting and calibration of post-bomb <sup>14</sup>C data. *Radiocarbon*, 46(3), 1299–1304. <https://doi.org/10.1017/S0038222000033154>
- Repasch, M., Scheingross, J. S., Hovius, N., Lupker, M., Wittmann, H., Haghpor, N., et al. (2021). Fluvial organic carbon cycling regulated by sediment transit time and mineral protection. *Nature Geoscience*, 14(11), 842–848. <https://doi.org/10.1038/s41561-021-00845-7>
- Ruff, M., Fahrni, S., Gäggeler, H. W., Hajdas, I., Suter, M., Synal, H.-A., et al. (2010). Elemental analyzer and micadas gas ion source. *Radiocarbon*, 52(4), 1645–1656. <https://doi.org/10.1017/s00382220005637x>
- Sanchez-Cabeza, J. A., & Ruiz-Fernández, A. C. (2012). <sup>210</sup>Pb sediment radiochronology: An integrated formulation and classification of dating models. *Geochimica et Cosmochimica Acta*, 82, 183–200. <https://doi.org/10.1016/j.gca.2010.12.024>
- Schuur, E. A. G., Trumbore, S. E., & Druffel, E. R. M. (2016). *Radiocarbon and climate change: Mechanisms, applications and laboratory techniques*. Springer. <https://doi.org/10.1007/978-3-319-25643-6>
- Shen, Z., Rosenheim, B. E., Törnqvist, T. E., & Lang, A. (2021). Engineered continental-scale rivers can drive changes in the carbon cycle. *AGU Advances*, 2(1), 1–16. <https://doi.org/10.1029/2020av000273>
- Soulet, G., Skinner, L. C., Beaupré, S. R., & Galy, V. (2016). A note on reporting of reservoir <sup>14</sup>C disequilibria and age offsets. *Radiocarbon*, 58(1), 205–211. <https://doi.org/10.1017/RDC.2015.22>
- Stuiver, M., & Polach, A. H. (1977). Discussion reporting of <sup>14</sup>C data. *Radiocarbon*, 19(3), 355–363. <https://doi.org/10.1017/s003822200003672>
- Sun, S., Meyer, V. D., Dolman, A. M., Winterfeld, M., Hefter, J., Dumann, W., et al. (2020). <sup>14</sup>C blank assessment in small-scale compound-specific radiocarbon analysis of lipid biomarkers and lignin phenols. *Radiocarbon*, 62(1), 207–218. <https://doi.org/10.1017/RDC.2019.108>
- Sun, X., Fan, D., Tian, Y., & Zheng, S. (2017). Normalization of excess <sup>210</sup>Pb with grain size in the sediment cores from the Yangtze River Estuary and adjacent areas: Implications for sedimentary processes. *The Holocene*, 28(4), 545–557. <https://doi.org/10.1177/0959683617735591>
- Synal, H. A., Stocker, M., & Suter, M. (2007). MICADAS: A new compact radiocarbon AMS system. *Nuclear Instruments and Methods in Physics Research, Section B: Beam Interactions with Materials and Atoms*, 259(1), 7–13. <https://doi.org/10.1016/j.nimb.2007.01.138>
- Syvitski, J., Ángel, J. R., Saito, Y., Overeem, I., Vörösmarty, C. J., Wang, H., & Olago, D. (2022). Earth's sediment cycle during the Anthropocene. *Nature Reviews Earth & Environment*, 3(3), 179–196. <https://doi.org/10.1038/s43017-021-00253-w>
- Syvitski, J. P. M., Vörösmarty, C. J., Kettner, A. J., & Green, P. (2005). Impact of humans on the flux of terrestrial sediment to the global coastal ocean. *Science*, 308(5720), 376–380. <https://doi.org/10.1126/science.1109454>
- Tao, S., Eglinton, T. I., Montluçon, D. B., McIntyre, C., & Zhao, M. (2015). Pre-aged soil organic carbon as a major component of the Yellow River suspended load: Regional significance and global relevance. *Earth and Planetary Science Letters*, 414, 77–86. <https://doi.org/10.1016/j.epsl.2015.01.004>
- Tao, S., Eglinton, T. I., Montluçon, D. B., McIntyre, C., & Zhao, M. (2016). Diverse origins and pre-depositional histories of organic matter in contemporary Chinese marginal sea sediments. *Geochimica et Cosmochimica Acta*, 191, 70–88. <https://doi.org/10.1016/j.gca.2016.07.019>
- Tian, Q. (2016). *Impacts of climate change and human activity on the water and sediment flux of the Yellow, Yangtze and Pearl River basins over the past 60 years*. East China Normal University.
- Torres, M. A., Limaye, A. B., Ganti, V., Lamb, M. P., Joshua West, A., & Fischer, W. W. (2017). Model predictions of long-lived storage of organic carbon in river deposits. *Earth Surface Dynamics*, 5(4), 711–730. <https://doi.org/10.5194/esurf-5-711-2017>
- Vonk, J. E., Drenzek, N. J., Hughen, K. A., Stanley, R. H. R., McIntyre, C., Montluçon, D. B., et al. (2019). Temporal deconvolution of vascular plant-derived fatty acids exported from terrestrial watersheds. *Geochimica et Cosmochimica Acta*, 244, 502–521. <https://doi.org/10.1016/j.gca.2018.09.034>
- Wacker, L., Němec, M., & Bourquin, J. (2010). A revolutionary graphitisation system: Fully automated, compact and simple. *Nuclear Instruments and Methods in Physics Research, Section B: Beam Interactions with Materials and Atoms*, 268(7–8), 931–934. <https://doi.org/10.1016/j.nimb.2009.10.067>

- Wei, B., Mollenhauer, G., Hefter, J., Grotheer, H., & Jia, G. (2020). Dispersal and aging of terrigenous organic matter in the Pearl River Estuary and the northern South China Sea shelf. *Geochimica et Cosmochimica Acta*, 282, 324–339. <https://doi.org/10.1016/j.gca.2020.04.032>
- Wei, B., Mollenhauer, G., Hefter, J., Kusch, S., Grotheer, H., Schefuß, E., & Jia, G. (2021a). The nature, timescale, and efficiency of riverine export of terrestrial organic carbon in the (sub)tropics: Insights at the molecular level from the Pearl River and adjacent coastal sea. *Earth and Planetary Science Letters*, 565, 116934. <https://doi.org/10.1016/j.epsl.2021.116934>
- Wei, B., Mollenhauer, G., Kusch, S., Hefter, J., Grotheer, H., Schefuß, E., et al. (2021b). Fatty acids and their carbon isotopes in two nearshore sediment cores from the coastal South China Sea [Dataset]. PANGAEA. <https://doi.pangaea.de/10.1594/PANGAEA.935797>
- Wu, C. S., Yang, S. L., & Lei, Y. P. (2012). Quantifying the anthropogenic and climatic impacts on water discharge and sediment load in the Pearl River (Zhujiang), China (1954–2009). *Journal of Hydrology*, 452(453), 190–204. <https://doi.org/10.1016/j.jhydrol.2012.05.064>
- Xu, S., Zhang, J., Wang, X., & Jia, G. (2016). Catchment environmental change over the 20th Century recorded by sedimentary leaf wax *n*-alkane  $\delta^{13}\text{C}$  off the Pearl River estuary. *Science China Earth Sciences*, 59(5), 975–980. <https://doi.org/10.1007/s11430-015-5206-3>
- Yang, C., Yang, S., Song, J., & Vigier, N. (2019). Progressive evolution of the Changjiang (Yangtze River) sediment weathering intensity since the three gorges dam operation. *Journal of Geophysical Research: Earth Surface*, 124(10), 2402–2416. <https://doi.org/10.1029/2019JF005078>
- Yao, P., Yu, Z., Bianchi, T. S., Guo, Z., Zhao, M., Knappy, C. S., et al. (2015). A multiproxy analysis of sedimentary organic carbon in the Changjiang Estuary and adjacent shelf. *Journal of Geophysical Research: Biogeosciences*, 120(7), 1407–1429. <https://doi.org/10.1002/2014JG002831>
- Yao, Z. T., Ji, X. S., Sarker, P. K., Tang, J. H., Ge, L. Q., Xia, M. S., & Xi, Y. Q. (2015). A comprehensive review on the applications of coal fly ash. *Earth-Science Reviews*, 141, 105–121. <https://doi.org/10.1016/j.earscirev.2014.11.016>
- Yim, W. W. S., Huang, G., Fontugne, M. R., Hale, R. E., Paterne, M., Pirazzoli, P. A., & Ridley Thomas, W. N. (2006). Postglacial sea-level changes in the northern South China Sea continental shelf: Evidence for a post-8200 calendar yr BP meltwater pulse. *Quaternary International*, 145–146, 55–67. <https://doi.org/10.1016/j.quaint.2005.07.005>
- Yu, F., Zong, Y., Lloyd, J. M., Huang, G., Leng, M. J., Kendrick, C., et al. (2010). Bulk organic  $\delta^{13}\text{C}$  and C/N as indicators for sediment sources in the Pearl River delta and estuary, southern China. *Estuarine, Coastal and Shelf Science*, 87(4), 618–630. <https://doi.org/10.1016/j.ecss.2010.02.018>
- Yu, M., Eglinton, T. I., Haghypour, N., Montluc, D. B., Wacker, L., Wang, Z., et al. (2019). Molecular isotopic insights into hydrodynamic controls on fluvial suspended particulate organic matter transport. *Geochimica et Cosmochimica Acta*, 262(238), 78–91. <https://doi.org/10.1016/j.gca.2019.07.040>
- Yu, M., Eglinton, T. I., Haghypour, N., Montluçon, D. B., Wacker, L., Hou, P., et al. (2021). Contrasting fates of terrestrial organic carbon pools in marginal sea sediments. *Geochimica et Cosmochimica Acta*, 309(238), 16–30. <https://doi.org/10.1016/j.gca.2021.06.018>

## References From the Supporting Information

- Wei, B., Mollenhauer, G., Hefter, J., Kusch, S., Grotheer, H., Schefuß, E., & Jia, G. (2021). The nature, timescale, and efficiency of riverine export of terrestrial organic carbon in the (sub)tropics: Insights at the molecular level from the Pearl River and adjacent coastal sea. *Earth and Planetary Science Letters*, 565, 116934. <https://doi.org/10.1016/j.epsl.2021.116934>
- Bovee, R. J., & Pearson, A. (2014). Strong influence of the littoral zone on sedimentary lipid biomarkers in a meromictic lake. *Geobiology*, 12(6), 529–541. <https://doi.org/10.1111/gbi.12099>
- Carreira, R. S., Araújo, M. P., Costa, T. L. F., Spörl, G., & Knoppers, B. A. (2011). Lipids in the sedimentary record as markers of the sources and deposition of organic matter in a tropical Brazilian estuarine-lagoon system. *Marine Chemistry*, 127(1–4), 1–11. <https://doi.org/10.1016/j.marchem.2011.07.002>
- Chikaraishi, Y., & Naraoka, H. (2007).  $\delta^{13}\text{C}$  and  $\delta\text{D}$  relationships among three *n*-alkyl compound classes (*n*-alkanoic acid, *n*-alkane and *n*-alkanol) of terrestrial higher plants. *Organic Geochemistry*, 38(2), 198–215. <https://doi.org/10.1016/j.orggeochem.2006.10.003>
- Matsumoto, G. I., Honda, E., Sonoda, K., Yamamoto, S., & Takemura, T. (2010). Geochemical features and sources of hydrocarbons and fatty acids in soils from the McMurdo Dry Valleys in the Antarctic. *Polar Science*, 4(2), 187–196. <https://doi.org/10.1016/j.polar.2010.04.001>
- Naraoka, H., & Ishiwatari, R. (2000). Molecular and isotopic abundances of long-chain *n*-fatty acids in open marine sediments of the western North Pacific. *Chemical Geology*, 165(1–2), 23–36. [https://doi.org/10.1016/S0009-2541\(99\)00159-X](https://doi.org/10.1016/S0009-2541(99)00159-X)
- Ratnayake, N. P., Suzuki, N., & Matsubara, M. (2005). Sources of long chain fatty acids in deep sea sediments from the Bering Sea and the North Pacific Ocean. *Organic Geochemistry*, 36(4), 531–541. <https://doi.org/10.1016/j.orggeochem.2004.11.004>
- Summons, R. E., Bird, L. R., Gillespie, A. L., Pruss, S. B., Roberts, M., & Sessions, A. L. (2013). Lipid biomarkers in ooids from different locations and ages: Evidence for a common bacterial flora. *Geobiology*, 11(5), 420–436. <https://doi.org/10.1111/gbi.12047>
- Volkman, J. K., Revill, A. T., Holdsworth, D. G., & Fredericks, D. (2008). Organic matter sources in an enclosed coastal inlet assessed using lipid biomarkers and stable isotopes. *Organic Geochemistry*, 39(6), 689–710. <https://doi.org/10.1016/j.orggeochem.2008.02.014>
- Makou, M., Eglinton, T., McIntyre, C., Montluçon, D., Antheaume, I., & Grossi, V. (2018). Plant wax *n*-alkane and *n*-alkanoic acid signatures overprinted by microbial contributions and old Carbon in meromictic lake sediments. *Geophysical Research Letters*, 45(2), 1049–1057. <https://doi.org/10.1002/2017GL076211>